Validation of an integrated satellite-data-driven response to an effusive crisis: the April–May 2018 eruption of Piton de la Fournaise

Andrew J.L. J.L. Harris, Magdalena Oryaëlle Chevrel, Diego Coppola, Michael Ramsey, Alexis Hrysiewicz, Simon Thivet, Nicolas Villeneuve, Massimiliano Favalli, Aline Peltier, Philippe Kowalski, et al.

ISTITUTO NAZIONALE DI GEOFISICA E VULCANOLOGIA

ACCEPTED ON ANNALS OF GEOPHYSICS, 61, 2018; Doi: 10.4401/ag-7972

Validation of an integrated satellite-data-driven response to an effusive crisis: the April–May 2018 eruption of Piton de la Fournaise

Andrew J.L. Harris[1], Magdalena Oryaelle Chevrel[1], Diego Coppola[2], Michael S. Ramsey[3], Alexis Hrysiewicz[1], Simon Thivet[1], Nicolas Villeneuve[4], Massimiliano Favalli[5], Aline Peltier[6], Philippe Kowalski[6], Andrea Di Muro[6], Jean-Luc Froger[1], Lucia Gurioli[1]

[1] Universite Clermont Auvergne, CNRS, OPGC, Laboratoire Magmas et Volcans, 63000 Clermont- Ferrand, France.

[2] Dipartimento di Scienze della Terra, Universita degli Studi di Torino, Via Valperga Caluso 35, 10125 Torino, Italy.

[3] Department of Geology and Planetary Science, University of Pittsburgh, Pittsburgh, PA, USA

[4] Laboratoire GeoSciences Reunion, Universite de La Reunion, Institut de Physique du Globe de Paris, Sorbonne Paris Cite, CNRS, F-97744 Saint Denis, France.

[5] Istituto Nazionale di Geofisica e Vulcanologia (INGV), Via della Faggiola, 32, 56126 Pisa, Italy.

[6] Observatoire Volcanologique du Piton de la Fournaise (OVPF), Institut de Physique du Globe de Paris, Sorbonne Paris Cite, Univ. Paris Diderot, CNRS, F-97418 La Plaine des Cafres, La Reunion, France.

Validation of an integrated satellite-data-driven response to an effusive crisis: the April–May 2018 eruption of Piton de la Fournaise

Andrew J.L. Harris[1], Magdalena Oryaëlle Chevrel[1], Diego Coppola[2], Michael S. Ramsey[3], Alexis Hrysiewicz[1], Simon Thivet[1], Nicolas Villeneuve[4], Massimiliano Favalli[5], Aline Peltier[6], Philippe Kowalski[6], Andrea Di Muro[6], Jean-Luc Froger[1], Lucia Gurioli[1]

1. Université Clermont Auvergne, CNRS, OPGC, Laboratoire Magmas et Volcans, 63000 Clermont-Ferrand, France.

2. Dipartimento di Scienze della Terra, Università degli Studi di Torino, Via Valperga Caluso 35, 10125 Torino, Italy.

3. Department of Geology and Planetary Science, University of Pittsburgh, Pittsburgh, PA, USA

4. Laboratoire GéoSciences Réunion, Université de La Réunion, Institut de Physique du Globe de Paris, Sorbonne Paris Cité, CNRS, F-97744 Saint Denis, France.

5. Istituto Nazionale di Geofisica e Vulcanologia (INGV), Via della Faggiola, 32, 56126 Pisa, Italy.

6. Observatoire Volcanologique du Piton de la Fournaise (OVPF), Institut de Physique du Globe de Paris, Sorbonne Paris Cité, Univ. Paris Diderot, CNRS, F-97418 La Plaine des Cafres, La Réunion, France.

Abstract. Satellite-based surveillance of volcanic hot spots and plumes can be coupled with modeling to allow ensemble-based approaches to crisis response. We complete benchmark tests on an effusive crisis response protocol aimed at delivering product for use in tracking lava flows. The response involves integration of four models: MIROVA for discharge rate (TADR), the ASTER urgent response protocol for delivery of high-spatial resolution satellite data, DOWNFLOW for flow path projections, and PyFLOWGO for flow run-out. We test the protocol using the data feed available during Piton de la Fournaise's April–May 2018 eruption, with product being delivered to the Observatoire du Piton de la Fournaise via Google Drive. The response was initialized by an alert at 19:50Z on 27 April 2018. Initially DOWNFLOW-FLOWGO were run using TADRs typical of Piton de la Fournaise, and revealed that flow at >120 m^3/s could reach the island belt road. The first TADR (10–20 m^3/s) was available at 09:55Z on 28 April, and gave flow run-outs of 1180–2510 m. The latency between satellite overpass and TADR provision was 105 minutes, with the model result being posted 15 minutes later. An InSAR image pair was completed six hours after the eruption began, and gave a flow length of 1.8 km; validating the run-out projection. Thereafter, run-outs were updated with each new TADR, and checked against flow lengths reported from InSAR and ASTER mapping. In all, 35 TADRs and 15 InSAR image pairs were processed during the 35-day-long eruption, and 11 ASTER images were delivered.

Introduction

Throughout the 1990's and 2000's methods were developed to extract lava flow discharge rates from 1 km spatial resolution satellite data collected by satellite sensors operating in the thermal infrared (e.g., Harris et al., 1997; 2007; Harris & Bologa 2009; Coppola et al., 2010). At the same time, high spatial resolution (30 m) satellite data were shown to be of value for mapping lava flow fields (e.g.,

Flynn et al., 1994; Wright et al., 2000; Lombardo et al., 2009), with InSAR data allowing estimation of lava flow areas, thicknesses and, hence, volumes (e.g., Zebker et al., 1996; Rowland et al., 1999; Lu et al., 2003). In parallel, a series of lava flow models were developed to allow flow inundation areas to be simulated (e.g., Young & Wadge, 1990; Crisci et al., 2003; Vicari et al., 2007). Increasingly, the capabilities have been merged to allow an ensemble-based approach whereby satellite data from multiple wavelengths and spatial resolutions are combined to allow maximum constraint and cross-validation (e.g., Patrick et al., 2003; Rowland et al., 2003; Wright et al., 2005) and source term input into real-time lava flow emplacement models (e.g., Wright et al., 2008; Vicari et al., 2011; Ganci et al., 2016). Since 2015, just such a response model has been developed at Piton de la Fournaise (Harris et al. 2017), where we here review and validate an updated version of the protocol so as to review an ensemble approach to responding to an effusive crisis.

The response protocol is based on *in situ* observations and data acquisitions carried out routinely by the Observatoire du Piton de la Fournaise (OVPF) team and the integration of four models: MIROVA (Coppola et al. 2016), the ASTER (Advanced Spaceborne Thermal Emission Radiometer) urgent response protocol (Ramsey, 2016), DOWNFLOW (Favalli et al., 2005) and FLOWGO (Harris and Rowland, 2001). MIROVA is a near-real time hot spot detection system that uses MODIS data, and has been calibrated for TADR calculation at Piton de la Fournaise by Coppola et al. (2010), the ASTER urgent response protocol is a means of automatically prioritizing and targeting ASTER data acquisition during a volcanic eruption. Instead, while DOWNFLOW is a stochastic model that assesses potential flow paths based on iterative runs over a DEM with random noise added, FLOWGO can calculate the cooling-limit of flow down each path (Rowland et al., 2005; Wright et al., 2008). To estimate the maximum distance a flow can extend at a given effusion rate, FLOWGO tracks the thermal and rheological evolution of a control volume of lava as it moves down a channel, tracking the volume until the volume cools and crystallizes to such an extent that forward motion becomes rheologically impossible (Harris and Rowland 2015). FLOWGO has been initialized for and tested for lava channels at Piton de la Fournaise by Harris et al. (2016) and Rhéty et al. (2017), and—to allow improved model initialization, iteration and application—has been rewritten and rebuilt in Python as PyFLOWGO (Chevrel et al., 2018). It is this version of FLOWGO that we use here.

As described in Harris et al. (2017), the response protocol is initialized with the alert of an imminent eruption and provision of the vent location provided by the OVPF as part of their mandated monitoring and response procedures. Subsequently, it involves calling each model in sequence and passing results between each actor, and then final product to OVPF, in as timely fashion as possible. The protocol also calls in ground truth (for vent locations, effusion rates, channel dimensions, flow lengths) provided by the OVPF as well as textural and chemical data (for eruption temperatures, vesicularity, crystallinity, rheological models) produced at LMV, to improve model uncertainty and syn-response validation. We show here how the response protocol works, and define the main uncertainties, using a real-time exercise held immediately after the April–May 2018 eruption of Piton de la Fournaise. The aim of the exercise was to refine model initialization and execution for Piton de la Fournaise, reduce uncertainty, and to fully define the call-down and communication protocol. It involved first following the data feed and executing responses, in the order that they were received, followed by a validation phase in which remote sensing and model based estimates for discharge rate and flow length were compared against ground truth. In doing so, we show how an integrated multi-sensor remote sensing approach can be used to follow, document and quantify an effusive event in near-real time.

The April–May 2018 eruption of Piton de la Fournaise and available data

The April–May 2018 eruption of Piton de la Fournaise began late on 27 April (19h50 UTC) from five north-south orientated en-echelon fissures that opened between the elevations of 2165 m and 2285 m on the southwest flank of the terminal cone (Figure 1a). Initially flow was channel-fed 'a'a which moved down the SW flank of the Dolomieu. In a short time activity reached a peak and became focused at a main vent roughly central to the fissure line at an elevation of 2200 m. Another much less active vent a few meters to the north continued to project tephra and emit flames. Around the two vents, scoria cones and tephra fields were constructed. Upon reaching the base of the Enclos Fouqué wall (between the 29 and 30 April), lava flows turned southeast to follow the base of the wall reaching a distance of 2.6 km before discharge rates declined and active flow fronts retreated to positions closer to the vent (Figure 1b). Between 4 and 7 May, flow activity was concentrated in the proximal section of the flow field with several tubes and, with two main zones of breakout being active 200 and 500 m down the tube system (Figure 1c). Breakouts from the tube system fed low-discharge rate flows which extended no more that 100–200 m. From 7 May new lava flows broke out from an ephemeral vent at the base of the Enclos Fouqué Southern wall producing local vegetation fires. Over the following days, the tube continued to extend and feed lava flows from its terminus, so that by 10 May the tube exit was around 3.2 km from the vent. This continued to feed low-discharge rate flows that extended over 1.1 km (or 4.5 km from the main vent) along the base of the Enclos Fouqué wall. Activity continued in this way until 1 June 2018 when activity died out around 14h30 (local time). During the 34.6-day-long eruption, six aerial photograph, two aerial IR image and several field observation campaigns, including GPS measurements, lava and tephra sampling, gas analysis and UAV over flights were completed by the OVPF. In addition, 35 cloud-free MODIS images, 11 ASTER images and 15 InSAR image pairs all of which were available for near-real time analysis and reporting.

Methodology

While implementation of MIROVA and the ASTER urgent response protocol (URP) allow near-real time collection and processing of satellite thermal data for derivation of time-averaged discharge rate and mapping of a thermal anomaly, DOWNFLOW and FLOWGO (DOWNFLOWGO) allow the flow paths and potential run out distance to be projected. These models are called in sequence, where the call-down procedure is given in Figure 2. As part of this system, output and product are shared using a standardized reporting form (as given in Appendix A) which is shared between an email distribution list involving all actors in the response chain, and to OVPF for integration into surveillance and reporting duties. With each update, the group is issued an update email, flagging the field that has been updated and giving the time and date of the update as well as the name of the person responsible for the update. The reporting form has four fields for: (i) current MIROVA-derived TADR and time series; (ii) current vent location and DOWNFLOWGO projections; (iii) current ASTER thermal distribution map, with flow field evolution time series and report; (iv) InSAR-based flow length report and coherence images (Appendix A). Another field may be added to the reporting form including relevant OVPF data collection, e.g., flow length from Structure from Motion (SfM), SO2 flux, sampling locations etc. This is left at the observatory's discretion to add depending on work loads and time commitment.

MIROVA and ASTER were called using the observatory bulletin announcing implementation of alert level 1, that is an eruption is believed (on the basis of seismic and ground deformation data) to be "imminent" (in the next minutes/hours). This causes ASTER to be targeted, and MIROVA to set up a "watch" for the first sign of a hot spot. Upon eruption onset, DOWNFLOWGO is run as soon as vent location(s) (GPS coordinates) is (are) known. The first vent location is usually provided by OVPF personnel or gendarmerie using hand-held GPS from a helicopter which is flown by the police (gendarmerie) service. Precision may vary depending on flight time available, the height of the fountains and the number of aircraft in the air space above the eruption site. Initially, to give an immediate idea of likely flow paths and inundation areas, 10000 flow lines are run to the edge of the DEM (i.e., the coast) over the most recent 5-m DEM with random noise of between ±0.8 m and ±2.5 m being added between each run. The slope from the line of steepest descent (LoSD) at ±0.001 m is then extracted (and smoothed every 10 m) and used for preliminary FLOWGO runs at various effusion rates (10, 20, 30, 40, 50, to 100 m^3/s). To do this, FLOWGO is initialized prior to the call down using typical Piton de la Fournaise thermo-rheological conditions and textural properties as given in Table 1. At the beginning of the eruption, a typical channel width of 4 m is taken (Table 1), and the model iterates on depth until the combination with calculated velocity gives the required effusion rate. Subsequently, upon derivation of a first TADR from MIROVA, the cooling-limited extent of flow down each flow line is then updated. Runs driven by the MIROVA-derived TADR are then plotted over a Piton de la Fournaise base map to give an idea of how the flow front may extend, or retreat, if TADRs increase (or decrease) over the current level. In addition, if vent location or channel width information are updated or made available, these are also modified and all models re-run.

Upon receipt of the first ASTER imagery a thermal anomaly map is produced, and flow locations and lengths assessed on the basis of the spatial distribution of spectral radiance in 90 m ASTER band 12 (thermal infrared, 8.925–9.275 μm). In addition, vent location is checked where the intense thermal anomaly at the vent is apparent in ASTER band 3 (near-infrared, 0.807 μm) image. The 15 m-pixel size, and one pixel accuracy of the geolocation, allows the location of the vent hot spot to ±15 m. This is often better than that provided by hand-held GPS, which when run in a fast moving helicopter records a point that will lag behind the craft point by several hundred meters. If this is the case, the vent location is updated and new DOWNFLOWGO runs are produced. If tubes begin to extend from the vent, this—following Wright et al. (2000)—becomes apparent in the high spatial resolution satellite images from the distribution of spectral radiance. In such as case, the source for DOWNFLOWGO will be moved to the tube exit.

In addition, InSAR interferograms and SfM data are processed for flow thickness and length maps that both add to the information flow and allow validation of model-based flow-length projections. Although remaining largely underutilized in an operational response sense, the value of such data in producing lava flow thickness maps as long been known (e.g., Zebker et al., 1996; Rowland et al., 1999; MacKay et al., 1998; Stevens, 2002; Lu et al., 2003), as has the potential for merging with ancillary data, such as thermal-IR-derived TADRs and model-based lava flow run-outs (Rowland et al., 2003). The InSAR method consists of computing an interferogram by subtracting the phase between two SAR images acquired for the same area at different times (for details of the method see Appendix B). These statistics which are input into a fourth field in the reporting form (Appendix A) and are also used to update the DEM used for flow path runs.

Validation

On 4 May 2018 an over flight was made in an ultra-light aircraft at a flight height of around 310 m above the ground surface. A thermal camera was used to collect 52 images of the lava flow field and vent system between 12:15 and 12:30 local time. The thermal camera was a FLIR Systems T650 which provides a 640 × 480 pixel image in the 8–14 μm waveband, with 0.65 mrad pixels. This, over a line-of-sight distance of 460 m (and viewing angle of 48°) gives a pixel size of 0.3 m. Images were used to obtain vent (eruption) temperatures and down channel surface temperature profiles to use in FLOWGO, as well as channel and flow dimensions plus radiative (Q_{rad}), convective (Q_{conv}) and total ($Q_{tot} = Q_{rad} + Q_{conv}$) heat fluxes to check against model output. In addition, the MODIS and ASTER images collected at 10:30 (local time) on the same day (i.e., two hours previously) were fitted to the thermal camera image mosaic to allow the heat fluxes and TADRs to be compared. TADR was extracted from the thermal camera images using $TADR = Q_{tot} / \rho (c_p \Delta T + f\Lambda)$, in which ρ is the lava density, c_p is specific heat capacity, ΔT is the cooling range, f is the fraction of crystals grown down flow and Λ is latent heat of crystallization. Values characteristic of recent lavas at Piton de la Fournaise were used for ρ, c_p, and f, these being 2079 kg/m^3, 1225 J/kg K and 0.1, respectively, with a cooling range of 75–250 °C (Harris et al. 2007). At the end of the eruption, following sample analysis, the chemical, temperature, crystallinity and vesicularity sections of the initialization file for flow modeling are checked, and if necessary, updated (Table 1).

Results

The trigger for the protocol of Figure 2 was the Bulletin released by OVPF on 27 April 2018 at 20h30 local time (16h30 UTC). The bulletin declared that a seismic crisis had begun at 20h15 local time (16h15 UTC) accompanied by rapid ground deformation indicative of "magma leaving the storage system and propagating towards the surface" (Peltier 2018). Consequently, an eruption was declared probable in the following minutes or hours, and the alert level was set to "Alert 1" (Peltier 2018). As a result, the MIROVA "watch" began at 20h30 (16h30 UTC) on 27 April, with an ASTER URP being triggered at 04h25 (00h25 UTC) on 29 April (Appendix C). In addition, on receipt of the Bulletin, DOWNFLOWGO was loaded with the most recent DEM of Piton de la Fournaise, this being the 5-m DEM generated from LiDAR data in 2010 modified by adding the largest flow fields in the area that are the October 2010 and the August 2015 using the InSAR-based thickness maps.

The eruption began at 23h50 local time (19h50 UTC) on 27 April. Initially DOWNFLOWGO was run from a vent location set on the basis of fissure location relative to pre-existing topographic features as apparent in images acquired by OVPF's web-cam monitoring network. For this case, the camera used was that of "Piton Bert" (BERC, http://www.ipgp.fr/fr/ovpf/reseau-de-cameras) which targets this sector of the volcano. Comparison of a daytime image as a background layer and an image acquired during the eruption revealed the fissure to approximately extend between two newly formed cinder cones at an elevation of 2200 m on the SW flank of the terminal cone. These cones were located at 365375 m E; 7649065 m S and 365500 m E; 7848455 m S, and DOWNFLOW was launched from a point between the two cones at 365377 m E; 7648853 m S. This showed that the flows would likely move SW down the flank of the terminal cone, and then turn SE to following the caldera wall to the coast (Figure 3). The effusion rate contour map for this case was subsequently produced and posted on the reporting form (Figure 3). This revealed that flows fed at sustained rates in excess of 120 m^3/s were capable of reaching the island belt road, to reach the coast.

However, because a 4 km wide basin existed after a distance of 4 km from the vent, flows became held up at this point, with even flows at 80 m^3/s coming to a halt 4 km from the vent; and to push the model across the basin needed more than 120 m^3/s. Thus, in reality, our prediction was that either time would be needed to fill this basin, where lava needed time spread and pile up, and/or for a tube to develop across the basin—a little like the case of lava flow advance towards Etnea Zafferana in 1992 (Barberi et al. 1993).

The first cloud-free MODIS overpass occurred at 09h55 (UTC, 13h55 local time) on 28 April, i.e., around 14 hours after the eruption began. This yielded a TADR of 10–20 m^3/s (Table 2). These values were immediately input into the reporting sheet, thereby being handed onwards for input into the PyFLOWGO initialization file. The first lava flow projection map was thus also completed and posted; revealing flows were capable of extending up to 1180–2510 m under initial conditions (Figure 4a). The latency between satellite overpass and TADR provision was 105 minutes, with the model result being posted 15 minutes later. The first S1B InSAR image pair was completed around six hours after the eruption began and was also entered into the reporting sheet (Figure 5a). These revealed that the flow was already 1.8 km long and covered an area of $0.5\pm0.1 \times 10^6$ m^2 (Table 3); giving an initial extension rate of around 5 m/min and coverage rate of 1400 ²/min. On the same day, at 09h00 (local time), the first SfM survey was completed and by 16h00 (local time) approximate location of the fissures and flow outline from aerial images were published by the OVPF.

At 03h33 (UTC, 07h33 local time) on 30 April, after a new aerial visit of the eruption, the center of the main fissure was precisely given at 365365 m E; 7648810 m S. By this time, however, MODIS-derived TADR had declined to 3.7–6.9 m^3/s (Table 2). Updating PyFLOWGO revealed reduced run-outs of 0.7–1.0 km. The first cloud-free ASTER image was acquired on 2 May. This revealed an 11 pixel-long anomaly of saturated pixels orientated NE-SW on the south flank of the Dolomieu (Figure 6)—equivalent to a 990 m long zone of active lava (Table 4). The active vent was apparent as a single pixel hot spot in the 15-m near-infrared data and the vent location was updated to 365280 m E; 7648835 m S (Appendix D), with the TADR for this day being 3.6–4.6 m^3/s (Table 2). These details were updated in the reporting form, and the vent location for DOWNFLOWGO adjusted slightly (although this had no effect on the flow paths or LoSD). The following day (3 May), the second coherence map was produced. This revealed that the lava flow field had, at some point, reached the base of the caldera wall, turning SE to follow the base of the wall (Figure 6) having attained a length of 2.5 km (Table 3). The shorter length of the active flows implied by the size of the thermal anomaly in ASTER on 2 May, as well as the 17 pixel (1530 m) long zone of cooler pixels beyond the front of the main hot spot indicated that flow front locations had begun to retreat back up flow by this time.

The thermal camera imagery obtained from the over-flight of 4 May confirmed that activity had diminished, and comprised tube-fed breakouts of channel-fed 'a'a (Figure 1c). Two main breakouts were located where the southern breakout was fed by a 2 m-wide channel which fed a 110 m pad of 'a'a. Total heat flux from the breakout was 435±50 MW, which converted to a TADR of 0.61–1.65 m^3/s. ASTER imagery revealed that, by 9 May, the tube had extended 2430 m (Figure 6) to feed lava flows of around 1.4 km in length. At the same time, MIROVA revealed continued decline in TADR (Figure 7) to between 1 and 2 m^3/s. As a result, the vent location for DOWNFLOW was moved to the tube exit, which ASTER gave as being at 364685 m E; 7647090 m S, and FLOWGO run at 1.6 and 3.8 m^3/s (Table 2) with an updated channel width and eruption temperature (Table 1). This gave flow lengths of 1–2 km beyond the end of the tube system (Figure 4b).

Thereafter, TADRs remained at low levels (Figure 7) and the flow field continued to build parallel with the base of the caldera wall (Figure 5). TADRs of 0.8 m^3/s characteristic of the final week of the eruption (Table 2) gave flow lengths that extended just 1 km from the end of the tube (Figure 4b). The flow field (both predicted and measured) attained a final length of 4.1 km and area of 1.3±0.1 × 10^6 m^2 (Table 3), and a volume of 5.5±1.6 x 10^6 m^2 (Table 2). In all, 35 TADR sets were processed by MIROVA (Table 2), 15 image pairs were processed for coherence analysis (Table 3), 11 ASTER images were obtained using the ASTER URP (Table 4) and DOWNFLOWGO was launched three times as TADR and vent location changed. Additionally, six aerial photograph data sets, two aerial IR image surveys and multiple field observations, including lava and tephra sampling, gas analyses, UAV over flights were completed by the OVPF. The final reporting sheet, filled out with all derived values from this data set, is given in Appendix D.

Discussion

The aerial survey mapping of the flow field of 30 April allowed checking of the dimensions of the lava flow field derived from InSAR data; the center line length being 1.8 km (the same as that given by InSAR) and the area having excellent coincidence with the zone of incoherence obtained from the InSAR data. Likewise, dimensions of InSAR zones of incoherence, ASTER thermal anomalies and FLOWGO lengths are in excellent agreement (Figure 8). For example, the thermal anomaly in ASTER on 2 May revealed that flows had extended to a maximum distance of 2520 m in the proceeding days. This compares with the 2.5 km long zone of incoherence recorded by the InSAR pair processed the following day (3 May) and the 2510 m flow length generated by FLOWGO using the maximum TADRs obtained from MIROVA the first few days of the eruption. Closing the circle with validation of the FLOWGO run outs with good fits with dimensions of incoherence and thermal anomalies in InSAR and ASTER data gives us confidence in the source terms (including MIROVA-derived TADR) entered into the model. We next assess the uncertainty in those MIROVA-derived TADR, as well as the FLOWGO run-outs and errors due to DEM problems.

Validation of MIROVA-derived TADR

The image collected on 4 May by MODIS-MIROVA indicates a total radiant power (Q_{rad}) of 497±149 MW, corresponding to a total TADR of 2.6±0.6 m^3/s. Total radiant power is around 42 % of that measured for the south breakout on 4 May using the thermal camera (i.e., 209±20 MW). The TADR (1.13±0.52 m^3/s) obtained from the thermal image is also 43 % that of the MODIS-MIROVA, indicating confidence in the latter value and the conversion routine used. In this regard, MODIS-MIROVA uses the conversion $Q_{rad}/TADR = c_{Rad}$ (Coppola et al. 2010). For Piton de la Fournaise, Coppola et al. (2010) used thermal camera data for the May–June 2003 eruption to obain c_{Rad} of 2.5±1 × 10^8 J m^{-3}. The value of c_{Rad} obtained here is 2.3±1 × 10^8 J m^{-3} indicating that the conversion factor is stable, still holds and provides a TADR in good agreement with ground truth.

FLOWGO Uncertainty

To test uncertainty, we take our initial run of 28 April which was initialized with a TADR of 20 m^3/s and vary the source terms of Table 1 within reasonable limits. Using the generic source terms of Table 1, the model solved for a channel depth of 4 m give a distance of 2510 m (Figure 4a).

Our first uncertainty is in eruption temperature. Thermal camera imagery of the vent on 4 May yielded maximum temperatures of up to 1210±40 °C, a value which is suspiciously high. On 10 May, similarly suspicious temperatures of 1700 °C were recorded over a small skylight at the base of the main scoria cone. These temperatures are higher than the liquidus for Piton de la Fournaise and therefore cannot correspond to lava temperatures. However, nighttime observations revealed flames over the vent, so this appears to be a flame temperature, where the presence of the flame likely explains the intense thermal anomaly in the ASTER NIR band. Flame-free maxima were 1142±35 °C, consistent with temperatures obtained from the glass chemistry. If we update the eruption from 1114 °C temperature to 1142 °C (and readjust the channel dimension to balance for similar TADR) this increases the run out by just 30 m, revealing that a 3 % uncertainty in eruption temperature results in a 1 % uncertainty in run out.

Our second uncertainty is in bubble content and crystallinity and associated rheology models. Based on our analysis of lava samples from the 2015 channel, bubble content could be as high as 50 vol.% and phenocryst content as low as 1 vol.%. Because we use a simple two phase (fluid+crystals) mixture model bubble content effects the velocity equation through its effect on density, while the lower starting crystal content reduces the viscosity of the mixture. While increasing the vesicularity to 50 vol.% decreases run-out by 120 m (11 %), decreasing the phenocryst content to 1 vol.% increases run-out by 470 m (28 %).

The third uncertainty is on surface temperature which controls heat loss and hence cooling rate. We have used the typical effective radiation temperature approximated from the data of Flynn and Mouginis-Mark (1994) for a lava channel on Kilauea to initialize the model (Table 1). The thermal imagery of the south break out channel indicates that this may be a little low, where temperatures down the center line are 520–890 °C, with a mean and standard deviation of 740 °C and 80 °C. If we use this mean temperature for the effective radiation temperature, we have a flow length that decreases by 230 m (23 %).

Our final uncertainty is on channel width. If, for example, we reduce to a width of 2 m, depth and velocity have to increase to 1.1 m and 4.8 m/s to balance the TADR. This yields a runout of 2550 m or 46 % longer, so that an uncertainty on channel depth of 50 % yields uncertainty on runout of the same order. However, to extent uncertainties may cancel. If for example, we increase the vesicularity to 50 vol.% but decrease the phenocryst content to 1 vol.% we change the runout by just 50 m (for the same TADR). Likewise, if we decrease channel width to 2 m, but increase surface temperature to 740 °C we change the runout by 50 m. Thus, our error appears to be around 4-5 %, so that the error on a predicted runout of 3000 m, is just less than a few hundred meters.

DEM uncertainty

Until now, for the near real time response at the effusive crises at Piton de la Fournaise, DOWNFLOW was run on the SRTM DEM from 2005. When we first ran the DOWNFLOW simulation (in May), the LoSD was not south to the base of the Enclos Fouqué wall, but projected due East. It was not possible to simulate the actual flow path because post-2005 topography could not be accounted for. However, now that we have updated our flow projection by using the 5-m 2010 DEM to which lava flow fields from October 2010 and August 2015 (which were both in the southern area of the Enclos Fouqué) were added, the predicted path is south, moving around the western edge of the 2015 flow field, and to reach the wall before flowing to the east along its base. This was exactly the trajectory of

the flow. Note that although the eruptive fissures were located near and onto the February 2015 flow (on the distal part) we did not update the DEM with this lava flow as it did not interfere with the ongoing flow process. To model flows on a very active volcano, where topography is constantly changing, we thus need a DEM that is updated after each eruption, so as to reduce uncertainties on predicted flow inundation area.

To obtain the inundation area, DOWNFLOW needs to be calibrated to a specific scenario, and this is achieved by tuning N and Dh (Favalli et al. 2011). Previous simulations that were compared with real cases at Piton de la Fournaise showed that N=10000 and Dh of 2.5 m gives a good approximation of the proximal area around the Dolomieu, while a Dh of 0.8 m gives a better estimation of the lava flow distal, coastal zone. Subsequently, to obtain the LoSD, DOWNFLOW is first run with 1000 iterations at Dh=1 mm which allows pits and holes to be filled. This filled DEM is then used to obtain a second LoSD with N=1 and Dh=0.001). Down the LoSD a slope value is extracted every 10 m for use in PyFLOWGO. PyFLOWGO includes traps for cases where slope values are negative or zero, where the slope is recalculated at each step from the average of the five previous and five following positive and non-zero values down the LoSD (Chevrel et al. 2018). This allows FLOWGO to overcome small terrain irregularities, and to project across holes and pits as well as flat zones. The value of 10 m has been chosen from several simulations and seems to be the best suited value. Although precise DEMs are always preferred, we find we have to smooth the LoSD in order to obtained results in agreement with reality.

In the present case, the changes in vent location between the first estimation and the coordinates obtained in the field or from the satellite images did not change significantly. The effect on the predicted flow path was therefore minor and limited to within 100 m of the vent area. However, knowing, and moving to, the break out location of 9 May, was essential to predict the final flow length (at the given new TADR). The protocol we are offering here, that is sharing ASTER, MODIS, and DOWNFLOWGO allow a back and forth to update the vent location and is therefore of major improvement for correct estimation of the lava flow path and runout distance. In addition this protocol is of service to OVPF to aid in monitoring needs for lava flow field evolution allowing both crisis management and appraisal of need to evacuate ground based monitoring stations falling in flow paths.

Conclusion

With the near-real time availability of data from so many satellite-based sensors, as well as the immediate availability of ground truth through upload to internet-based data hubs, the best way forward to tracking an effusive crisis is an ensemble-based approach. Such a system is open to expansion and ingestion of further data sets to improve coverage and further reduce lags between event and measurement. For example, VIIRS (Visible Infrared Imaging Radiometer Suite) can be considered as an extension to MODIS (Blackett 2015), and Sentinel-2 as an extension to ASTER (Cappello et al. 2018), with other sensors being incorporated as they come on-line. In this regard, technology is constantly evolving with new potential coming-on line every year where, for this case, we have begun to convolve data from sensors flown on UAVs, as well as from crowdsourcing. Another developing avenue is small, low cost satellite networks, such as the small satellite Technology Experiment Carrier-1 (TET-1) as developed by the German Aerospace Center and dedicated to monitoring high temperature events (Zhukov et al. 2006). Such systems offer high

spatial resolution (160 m) thermal infrared imagery at a relatively high temporal resolution (3 days) and have shown to be of value in tracking effusive crises yielding TADR time series to supplement those provided by MODIS (Zakšek et al. 2005).

As shown here, merging thermal data of different resolutions allows time series generation with the best possible temporal resolution and precision; cross-validation of TADR, error and uncertainty assessment; and input into lava flow emplacement models. The next step will be the use of InSAR data to allow DEMs to be updated between eruptions so as to ensure that flow paths are correct and use the most up-to-date topography available, with the DEM evolving as the topography changes. This is a key feature, especially during a long-term eruption with changing topography and vent position. In turn, the chain can be inverted where good agreement of model-predicted flow lengths with dimensions of thermal and incoherence anomalies in high spatial resolution and thermal data suggests that the source terms input into the model are valid. Another key feature explored here is immediate delivery of a flow run out map that considers all feasible TADRs. This means that delivery of the hazard map, which can be created in a few minutes, does not have to be attendant on the first, cloud-free satellite overpass for delivery of a TADR. Instead, the map gives the hazard manager an immediate idea of possible event scenario's which can be assessed and checked when the first TADR comes in, and updated as vent locations and topographies change.

Acknowledgments. This work comes out of a three day workshop and exercise held in Clermont Ferrand in June 2018 funded by ANR-LAVA. This work was funded by the Agence National de la Recherche (ANR: www.agence-nationale-recherche.fr) through project ANR-LAVA (ANR Program: DS0902 2016; Project: ANR-16 CE39-0009, PI: A. Harris, Link: www.agence-nationale-recherche.fr/?Project=ANR-16-CE39-0009; https://sites.google.com/view/anrlava/). We would like to thank the Sentinel-1 ESA team, especially P. Potin and Y.-L. Desnos for having made possible routine Sentinel-1 StripMap acquisition on La Réunion Island. This is ANR-LAVA contribution no. 5 and IPGP contribution no. XXX.

References

Favalli M, Pareschi MT, Neri A, Isola I (2005) Forecasting lava flow paths by a stochastic approach. Geophys Res Lett, 32(L03305). doi: 10.1029/2004GL021718

Flynn LP, Mouginis-Mark PJ (1994) Temperature measurements of an active lava channel from spectral measurements, Kilauea Volcano, Hawaii. Bulletin of Volcanology, 56, 297-301

Harris AJL, Rowland SK (2001) FLOWGO: a kinematic thermo-rheological model for lava flowing in a channel. Bull Volcanol, 63, 20–44. doi:10.1007/s004450000120.

Harris AJL, Baloga SM (2009) Lava discharge rates from satellite-measured heat flux. Geophys. Res. Lett., 36, L19302. doi:10.1029/2009GL039717

Harris AJL, Rowland SK (2015) FLOWGO 2012: an updated framework for thermorheological simulations of channel-contained lava. In: Carey, R., Cayol, V., Poland, M., Weis, D. (Eds.),

413 Hawaiian Volcanoes: from Source to Surface, Geophysical Monograph, vol. 208. American
414 Geophysical Union, 457–481

415 Harris AJL, Blake S, Rothery DA, Stevens NF (1997) A chronology of the 1991 to 1993 Etna eruption
416 using AVHRR data: Implications for real time thermal volcano monitoring, J. Geophys. Res.,
417 102(B4), 7985–8003. doi:10.1029/96JB03388

418 Harris AJL, Dehn J, Calvari S (2007) Lava effusion rate definition and measurement: a review. Bull
419 Volcanol, 70, 1–22

420 Harris A, Rhéty M, Gurioli L, Villeneuve N, Paris R. (2016) Simulating the thermorheological evolution
421 of channel-contained lava: FLOWGO and its implementation in EXCEL. In: Harris AJL, De Groeve T,
422 Garel F, Carn SA, editors. Detecting, modelling and responding to effusive eruptions, vol. 426.
423 London: Geological Society, London Special Publication, 313–36. doi:10.1144/SP426.9.

424 Barberi F, Carapezz ML, Valenza M, Villari L (1993) The control of lava flow during the 1991–1992
425 eruption of Mt. Etna. Journal of Volcanology and Geothermal Research, 56(1–2), 1-34.

426 Blackett M (2015) An initial comparison of the thermal anomaly detection products of MODIS and
427 VIIRS in their observation of Indonesian volcanic activity. Remote Sensing of Environment, 171,
428 75-82

429 Cappello A, Ganci G, Bilotta G, Herault A, Zago V, Del Negro C (2018) Satellite-driven modeling
430 approach for monitoring lava flow hazards during the 2017 Etna eruption. Annals of Geophysics,
431 61, Doi:10.4401/ag-7792

432 Chevrel MO, Labroquère J, Harris AJL, Rowland SK (2018) PyFLOWGO: An open-source platform for
433 simulation of channelized lava thermo-rheological properties. Computers & Geosciences, 111,
434 167–180

435 Coppola D, James MR, Staudacher T, Cigolini C (2010) A comparison of field- and satellite-derived
436 thermal flux at Piton de la Fournaise: implications for the calculation of lava discharge rate. Bull
437 Volcanol., 72(3), 341–56. doi:10.1007/s00445-009-0320-8

438 Coppola D, Laiolo M, Cigolini C, Delle Donne D, Ripepe M (2016) Enhanced volcanic hot-spot
439 detection using MODIS IR data: results from the MIROVA system. In: Harris AJL, De Groeve T,
440 Garel F, Carn SA, editors. Detecting, Modelling and responding to effusive eruptions, vol. 426.
441 London: Geological Society, London, Special Publications, 181–205.
442 http://doi.org/10.1144/SP426.5.

443 Crisci G, Di Gregorio S, Rongo R, Scarpelli M, Spataro W, Calvari S (2003) Revisiting the 1669 Etnean
444 eruptive crisis using a cellular automata model and implications for volcanic hazard in the Catania
445 area. Journal of Volcanology and Geothermal Research, 123, 211-230.

446 Flynn LP, Mouginis-Mark PJ, Horton KA (1994) Distribution of thermal areas on an active lava flow
447 field: Landsat observations of Kilauea, Hawaii, July 1991. Bull. Volcanol., 56, 284-296.

448 Ganci G, Bilotta G, Cappello A, Herault A, Del Negro C (2016) HOTSAT: a multiplatform system for the
449 thermal monitoring of volcanic activity using satellite data. In Harris, A. J. L., De Groeve, T., Garel,

F. & Carn, S. A. (eds) 2016. Detecting, Modelling and Responding to Effusive Eruptions. Geological Society, London, Special Publications, 426, 207–221. First published online October 29, 2015, http://doi.org/10.1144/SP426.21

Lombardo V, Harris AJL, Calvari S, Buongiono MF (2009) Spatial variations in lava flow field thermal structure and effusion rate derived from very high spatial resolution hyperspectal (MIVIS) data. J. Geophys. Res., 114, B02208. doi:10/1029.2008JB005648

Lu Z, Fielding E, Patrick MR, Trautwein CM (2003) Estimating lava volume by precision combination of multiple baseline spaceborne and airborne interferometric synthetic aperture radar: The 1997 eruption of Okmok volcano, Alaska. IEEE Transactions on Geoscience and Remote Sensing ,41(6), I428-I436.

MacKay ME, Rowland SK, Mouginis-Mark PJ, Gareil H (1998) Thick lava flows of Karisimbi volcano, Rwanda: insights from SIR-C interferometric topography. Bull. Volcanol., 60, 239-251.

Patrick MR, Dehn J, Papp KR, Lu Z, Dean K, Moxey L, Izbekov P, Guritz R (2003) The 1997 eruption of Okmok Volcano, Alaska: a synthesis of remotely sensed imagery. J Volcanol Geotherm Res, 127, 87–105

Peltier A (2018) Bulletin du 27 avril 2018 – 20:30 heure locale Observatoire Volcanologique du Piton de la Fournaise. Bulletin of the Observatoire Volcanologique du Piton de la Fournaise, 27 April 2018, OVPF_20180427_20h30- *ISSN 2610-5101.*

Ramsey M (2016) Enhanced volcanic hot-spot detection using MODIS IR data: results from the MIROVA system. In: Harris AJL, De Groeve T, Garel F, Carn SA, editors. Detecting, Modelling and responding to effusive eruptions, vol. 426. London: Geological Society, London, Special Publications, 181–205. http://doi.org/10.1144/SP426.5.

Rhéty M, Harris A, Villeneuve N, Gurioli L, Médard E, Chevrel O, Bachélery P (2017) A comparison of cooling-limited and volume-limited flow systems: Examples from channels in the Piton de la Fournaise April 2007 lava-flow field, Geochem. Geophys. Geosyst., 18, doi:10.1002/2017GC006839.

Rowland SK, MacKay ME, Garbeil H, Mouginis-Mark PJ (1999) Topographic analyses of Kilauea volcano, Hawaii, from interferometric airborne radar. Bull. Volcanol., 61, 1-14.

Rowland SK, Harris AJL, Wooster MJ, Amelung F, Garbeil H, Wilson L, Mouginis-Mark PJ (2003) Volumetric characteristics of lava flows from interferometric radar and multispectral satellite data: the 1995 Fernandina and 1998 Cerro Azul eruptions in western Galápagos. Bull. Volcanol., 65, 311-330.

Rowland SK, Garbeil H, Harris A (2005) Lengths and hazards from channel-fed lava flows on Mauna Loa, Hawai'i, determined from thermal and downslope modeling with FLOWGO. Bull. Volcanol., 67, 634–647.

Stevens NF (2002) Emplacement of the large andesitic lava flow in the Oturere Stream valley, Tongariro Volcano, from airborne interferometric radar. New Zealand Journal of Geology and Geophysics, 45, 387-394.

Vicari A, Herault A, Del Negro C, Coltelli M, Marsella M, Proietti C (2007) Modeling of the 2001 lava flow at Etna volcano by a Cellular Automata approach. Environmental Modelling and Software, 22, 1464-1471.

Vicari A, Ganci G, Behncke B, Cappello A, Neri M, Del Negro (2011) Near-real-time forecasting of lava flow hazards during the 12–13 January 2011 Etna eruption. Geophysical Research Letters, 38, L13317. http://doi.org/10.1029/2011GL047545

Villeneuve N, Neuville DR, Boivin P, Bachèlery P, Richet P (2008) Magma crystallization and viscosity: a study of molten basalts from the Piton de la Fournaise volcano (La Réunion island). Chemical Geology, 256, 242–251

Wright R, Rothery DA, Blake S, Pieri DC (2000) Visualizing active volcanism with high spatial resolution satellite data: the 1991–1993 eruption of Mount Etna. Bull. Volcanol., 62, 256–265

Wright R, Carn SA, Flynn LP (2005) A satellite chronology of the May–June 2003 eruption of Anatahan volcano. Journal of Volcanology and Geothermal Research, 146, 102-116.

Wright R, Garbeil H, Harris AJL (2008) Using infrared satellite data to drive a thermorheological/stochastic lava flow emplacement model: A method for near-real-time volcanic hazard assessment. Geophys Res Lett., 35(L19307). doi:10.1029/2008GL035228

Zakšek K, Hort M, Lorenz E (2015) Satellite and Ground Based Thermal Observation of the 2014 Effusive Eruption at Stromboli Volcano. *Remote Sens., 7*, 17190-17211.

Zebker HA, Rosen P, Hensley S, Mouginis-Mark PJ (1996) Analysis of active lava flows on Kilauea volcano, Hawaii, using SIR-C radar correlation measurements. Geology, 24(6), 495-498.

Zhukov B, Lorenz E, Oertel D, Wooster M, Roberts G (2006) Spaceborne detection and characterization of fires during the bi-spectral infrared detection (BIRD) experimental small satellite mission (2001-2004). Remote Sens. Environ., 100, 29–51

Young P, Wadge G (1990). FLOWFRONT: Simulation of a lava flow. Computers and Geosciences, 16, 1171-1191.

514 **Figure Captions**

515 Figure 1. Location of the vent for the April–May 2018 eruption on the Dolomieu cone overlain on
516 Google Earth with (a) MODIS, (b) ASTER and (c) thermal camera mosaic of the hot spots
517 associated with active lava flow on 4 May overlain. Yellow outline in (c) gives the limit of the flow
518 field as mapped using hand-held GPS.

519 Figure 2. Flow chart giving the call-down and reporting procedure, as well as flow of source terms,
520 between each model.

521 Figure 3. DOWNFLOW inundation area for a 10000 iterations from the initial vent location with DEM
522 noise (Dh) of 0.8 m (light blue) and 2.5 m (dark blue), with the line of steepest descent in red.
523 Yellow stars give the distance down the LoSD FLOWGO runs at each generic effusion rate
524 (numbers are in m^3/s). These are the "effusion rate contours" for this eruption.

525 Figure 4. Distance down the LoSD (red line) that FLOWGO will run at the given effusion rates, these
526 being the numbers (in m^3/s) next to each star. Runs are given from (a) the initial vent location of
527 28 April, and (b) the tube exit on 9 May. Overlain are the limits of the flow field defined from
528 InSAR incoherence (blue outline) and field mapping (yellow outline) on the same dates.
529 Background shows the DOWNFLOW inundation area.

530 Figure 5. Time-series of InSAR incoherence images with lava flow field outlined in blue.

531 Figure 6. Time-series of ASTER TIR images with active flows apparent as elongate thermal anomalies
532 (higher pixel-integrated temperatures give lighter tones: white are the hottest pixels, and black
533 are the coldest). Note how the highest intensities in the thermal anomaly move down flow with
534 time, and effect of lava tube extension.

535 Figure 7. MIROVA-derived TADR and cumulative volume.

536 Figure 8. Comparison of ASTER thermal anomaly, InSAR incoherence and FLOWGO run outs for (a) 4
537 May (FLOWGO run from the initial vent location) and (b) 9 May (FLOWGO run from the tube exit
538 along the new path, yellow line).

539

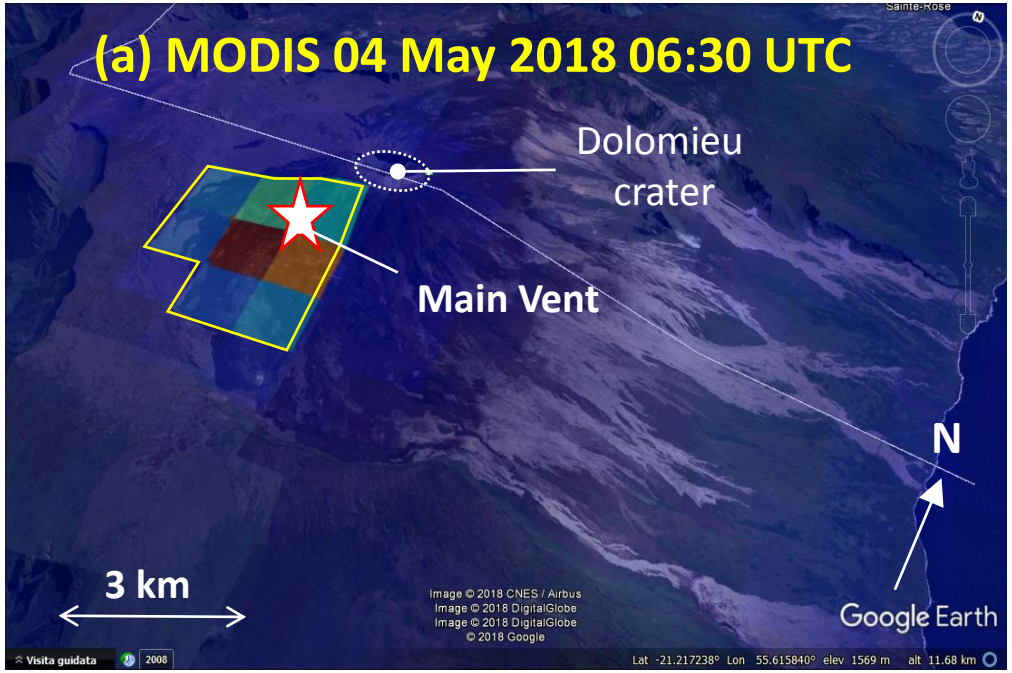
(a) MODIS 04 May 2018 06:30 UTC
Dolomieu crater
Main Vent
N
3 km
Image © 2018 CNES / Airbus
Image © 2018 DigitalGlobe
Image © 2018 DigitalGlobe
© 2018 Google
Google Earth

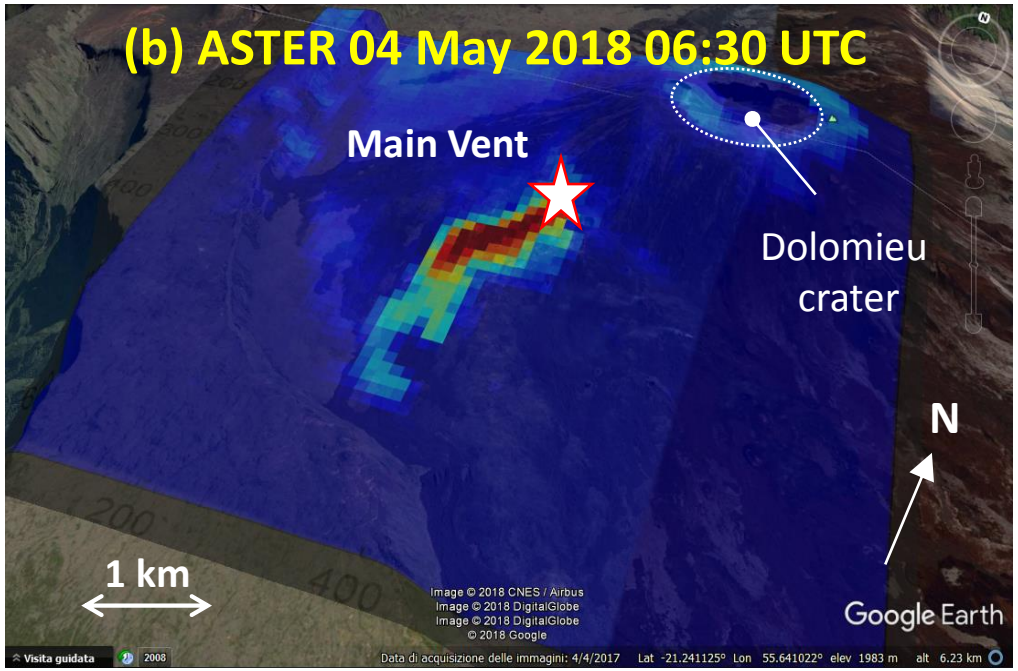
(b) ASTER 04 May 2018 06:30 UTC
Main Vent
Dolomieu crater
N
1 km
Image © 2018 CNES / Airbus
Image © 2018 DigitalGlobe
Image © 2018 DigitalGlobe
© 2018 Google
Google Earth

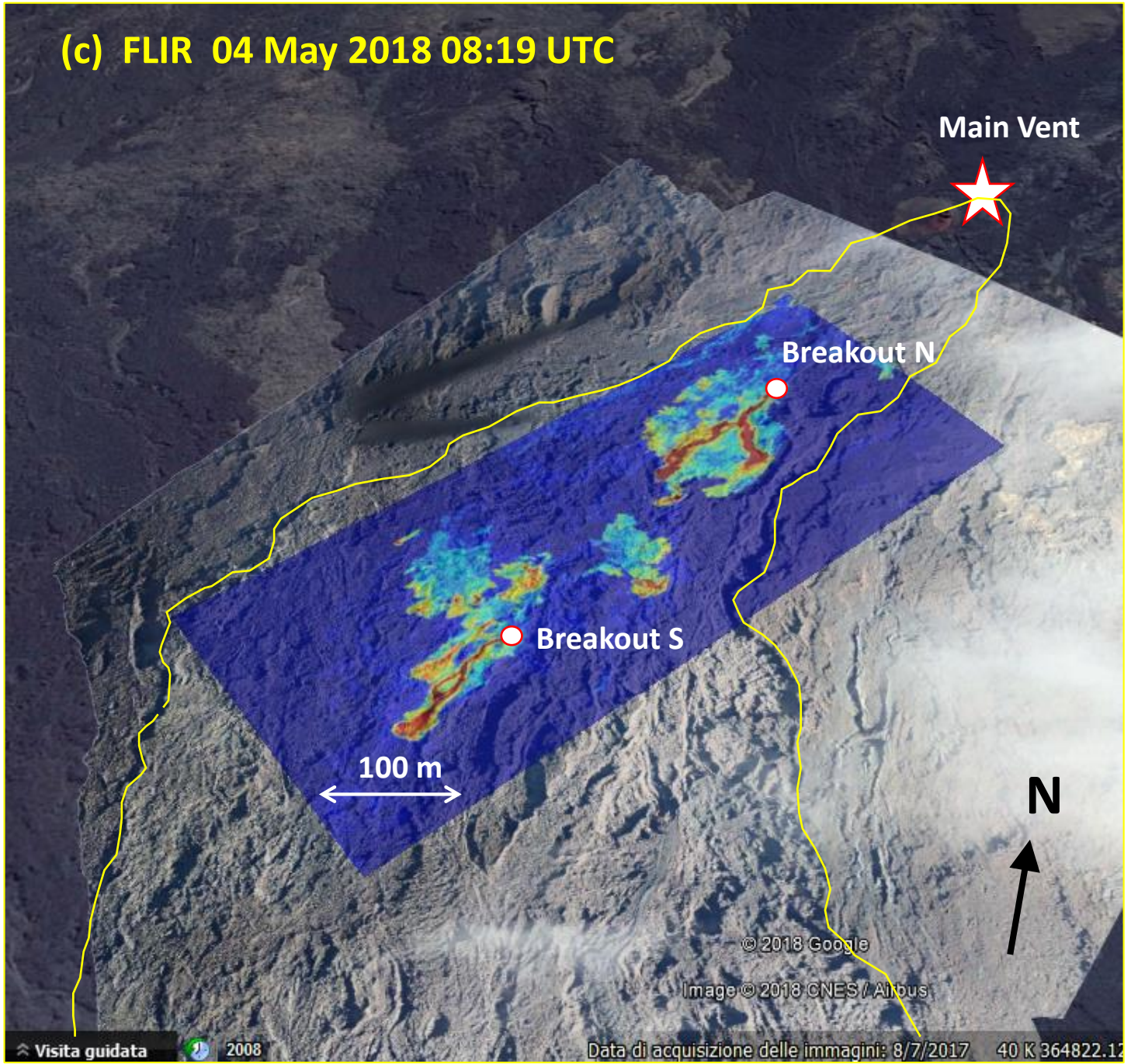
(c) FLIR 04 May 2018 08:19 UTC
Main Vent
Breakout N
Breakout S
100 m
N
© 2018 Google
Image © 2018 CNES / Airbus

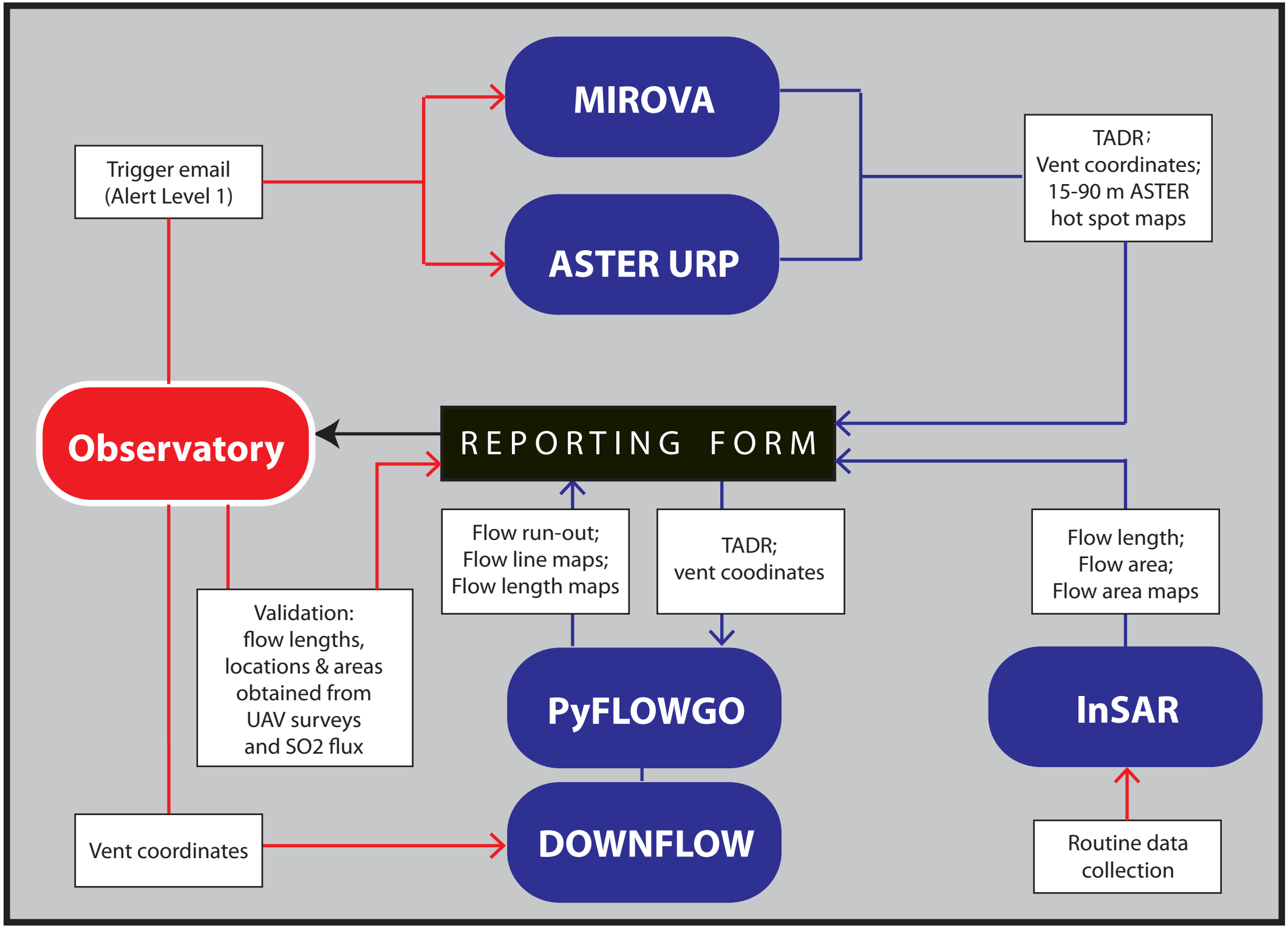
MIROVA
ASTER URP
Trigger email
(Alert Level 1)
TADR;
Vent coordinates;
15-90 m ASTER
hot spot maps
Observatory
REPORTING FORM
Flow run-out;
Flow line maps;
Flow length maps
TADR;
vent coodinates
Flow length;
Flow area;
Flow area maps
Validation:
flow lengths,
locations & areas
obtained from
UAV surveys
and SO2 flux
PyFLOWGO
InSAR
Vent coordinates
DOWNFLOW
Routine data
collection

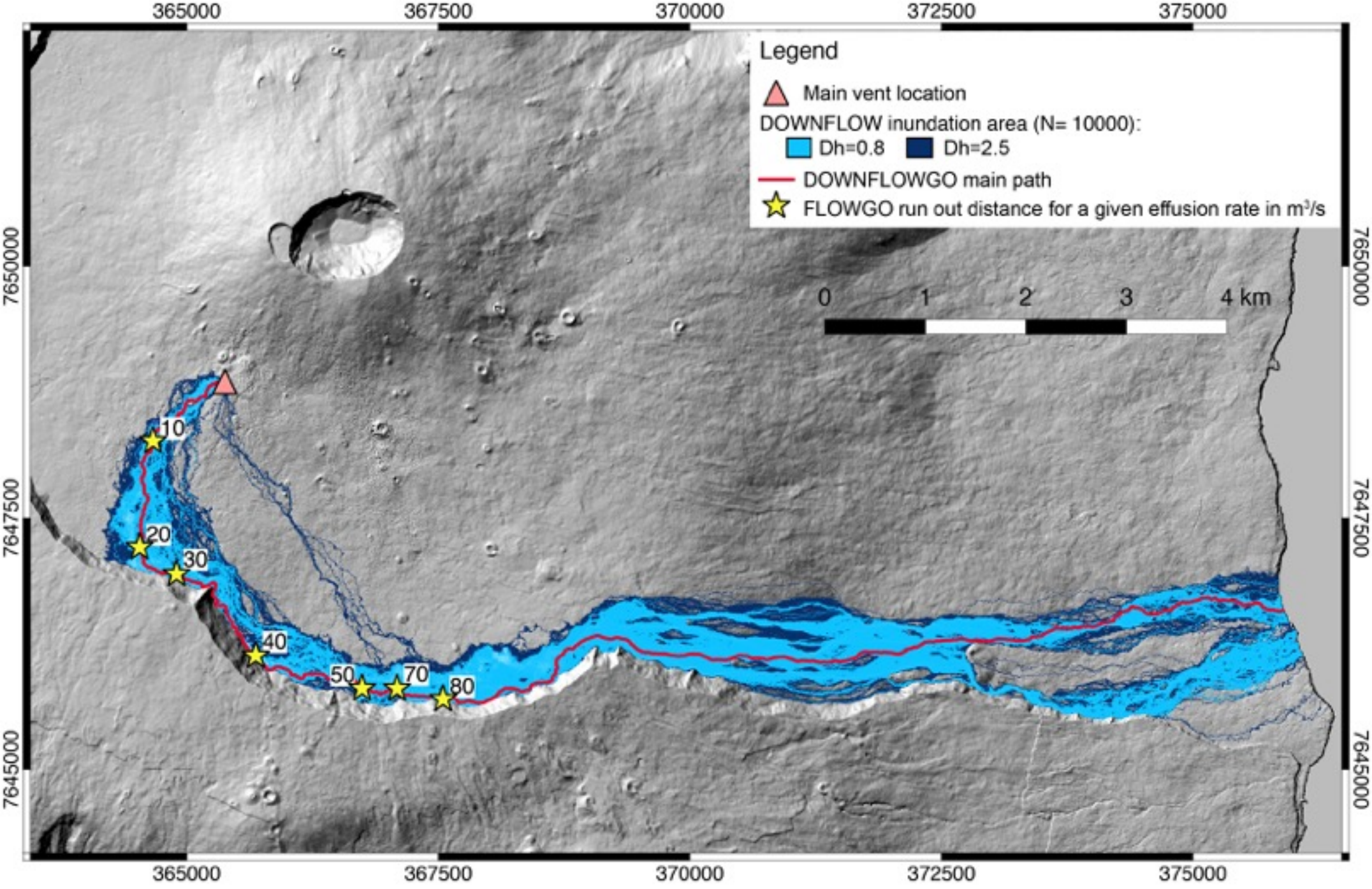
365000
367500
370000
372500
375000
7650000
7647500
7645000
Legend
Main vent location
DOWNFLOW inundation area (N= 10000):
Dh=0.8
Dh=2.5
DOWNFLOWGO main path
FLOWGO run out distance for a given effusion rate in m³/s
0
1
2
3
4 km
10
20
30
40
50
70
80

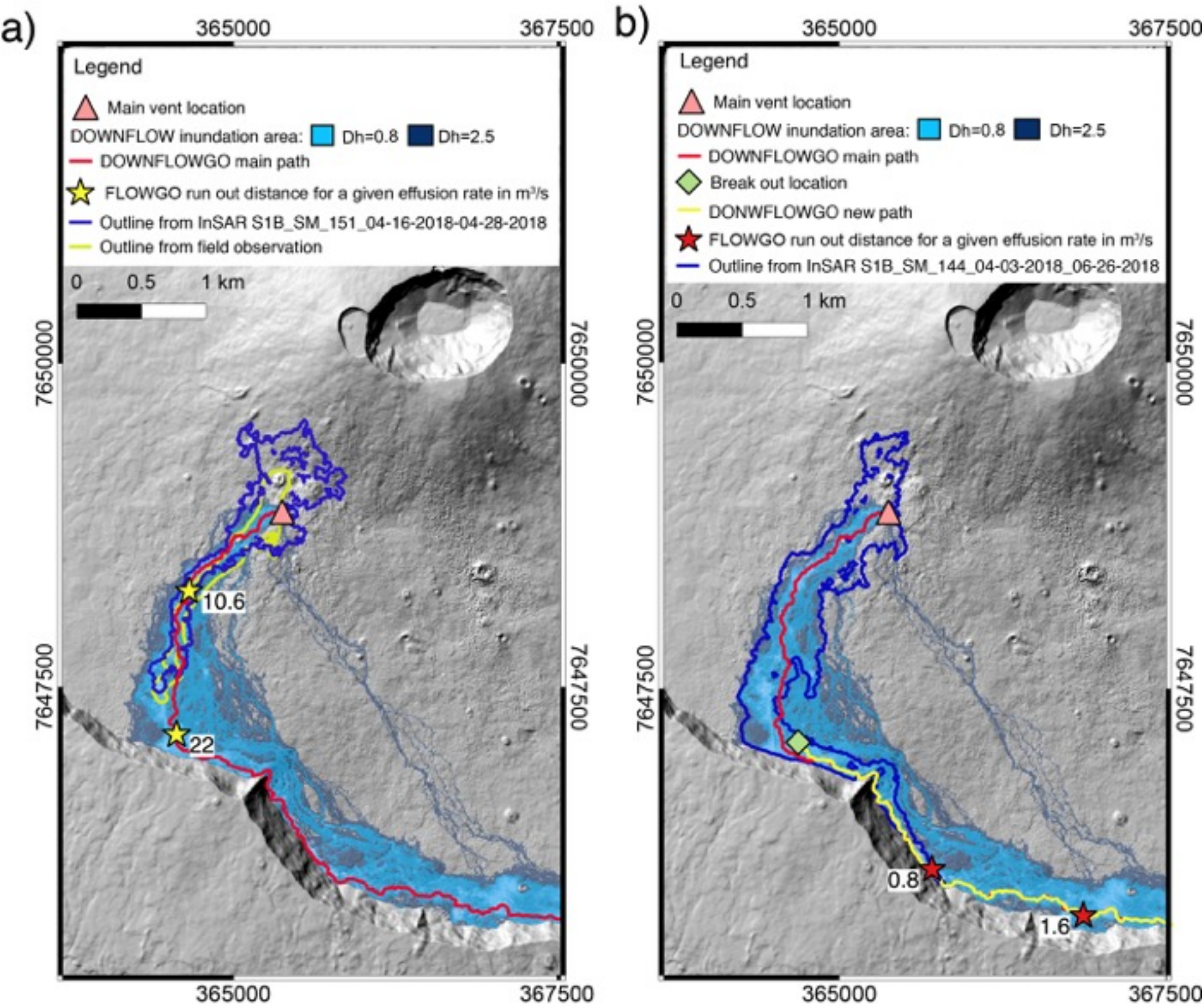
a)
b)
365000
367500
7650000
7647500
Legend
Main vent location
DOWNFLOW inundation area:
Dh=0.8
Dh=2.5
DOWNFLOWGO main path
FLOWGO run out distance for a given effusion rate in m³/s
Outline from InSAR S1B_SM_151_04-16-2018-04-28-2018
Outline from field observation
0 0.5 1 km
10.6
22
Break out location
DONWFLOWGO new path
Outline from InSAR S1B_SM_144_04-03-2018_06-26-2018
0.8
1.6

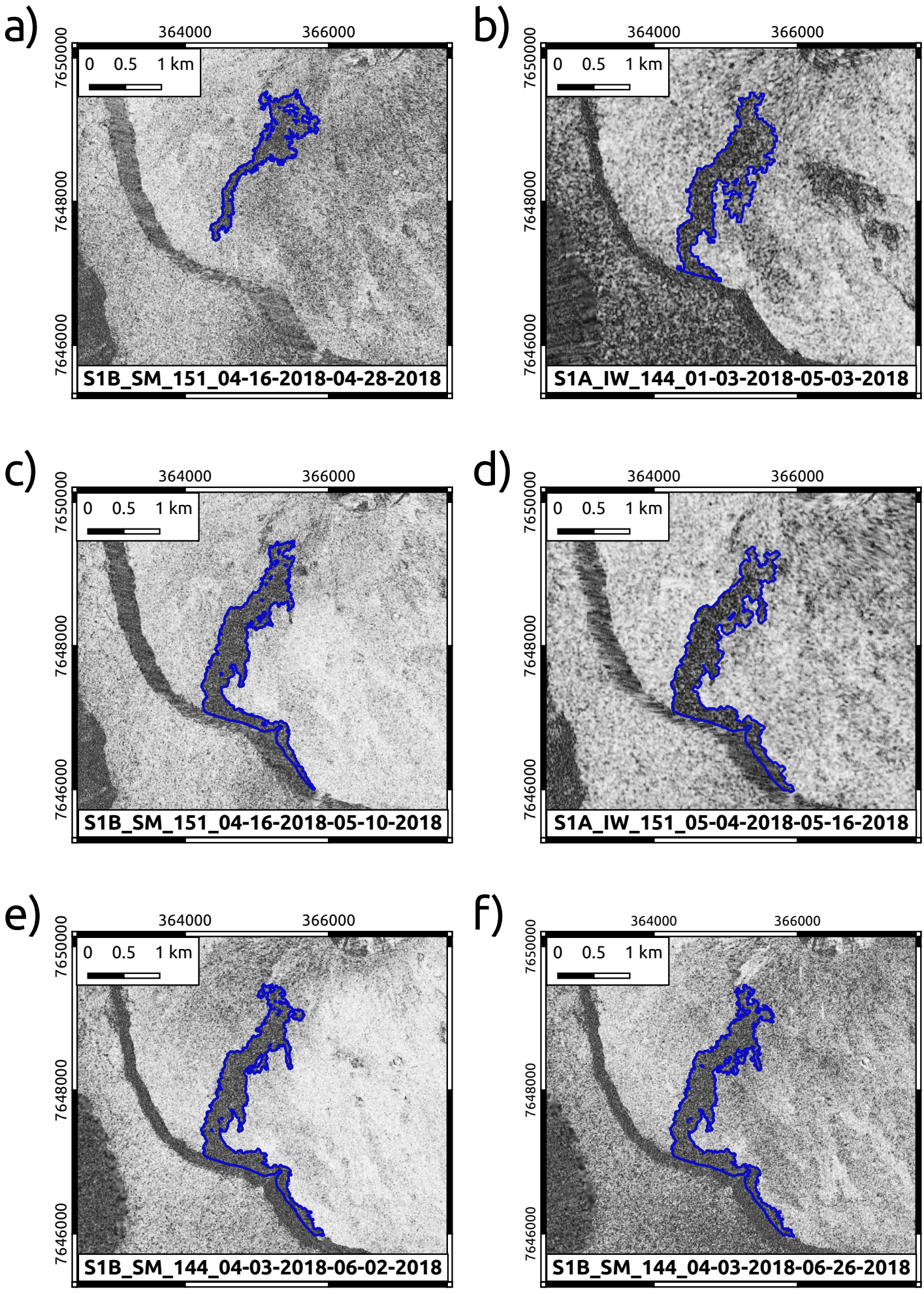
a)
b)
c)
d)
e)
f)
364000
366000
7650000
7648000
7646000
0 0.5 1 km
S1B_SM_151_04-16-2018-04-28-2018
S1A_IW_144_01-03-2018-05-03-2018
S1B_SM_151_04-16-2018-05-10-2018
S1A_IW_151_05-04-2018-05-16-2018
S1B_SM_144_04-03-2018-06-02-2018
S1B_SM_144_04-03-2018-06-26-2018
Coherence
0
0.25
0.5
0.75
1

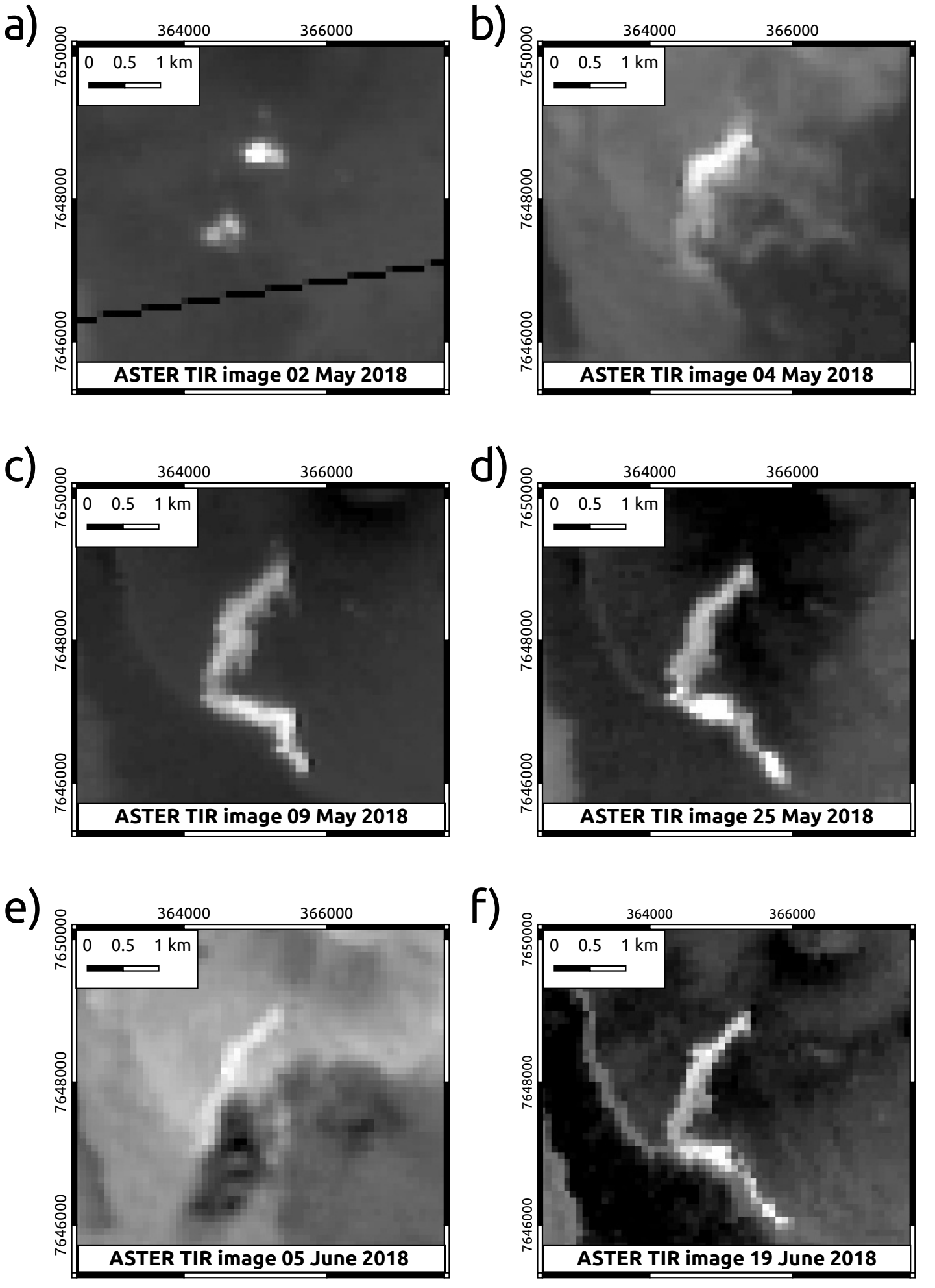
a)
b)
c)
d)
e)
f)
364000
366000
7650000
7648000
7646000
0 0.5 1 km
ASTER TIR image 02 May 2018
ASTER TIR image 04 May 2018
ASTER TIR image 09 May 2018
ASTER TIR image 25 May 2018
ASTER TIR image 05 June 2018
ASTER TIR image 19 June 2018
Temperature
Cold
Hot

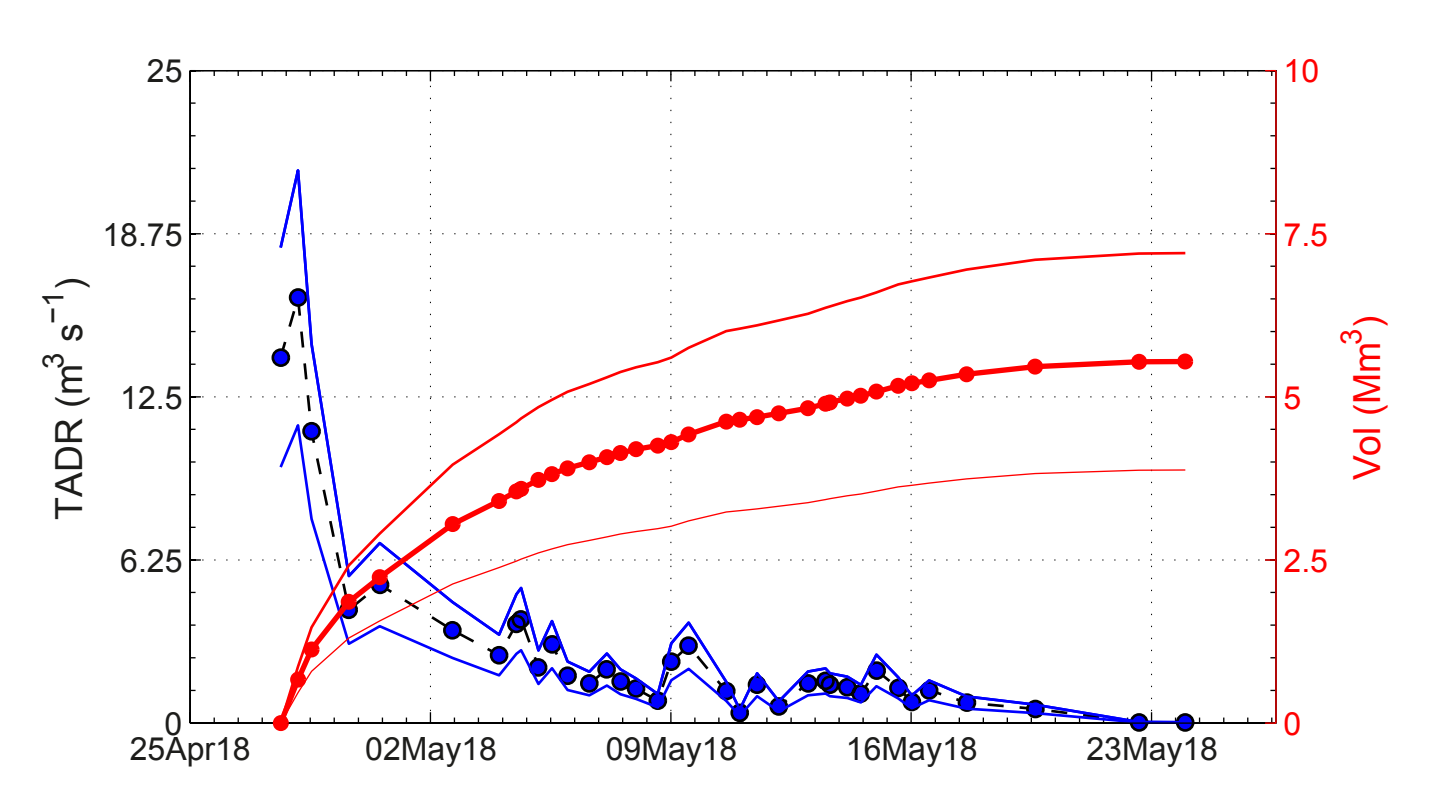
25
18.75
12.5
6.25
0
TADR (m3 s−1)
10
7.5
5
2.5
0
Vol (Mm3)
25Apr18
02May18
09May18
16May18
23May18

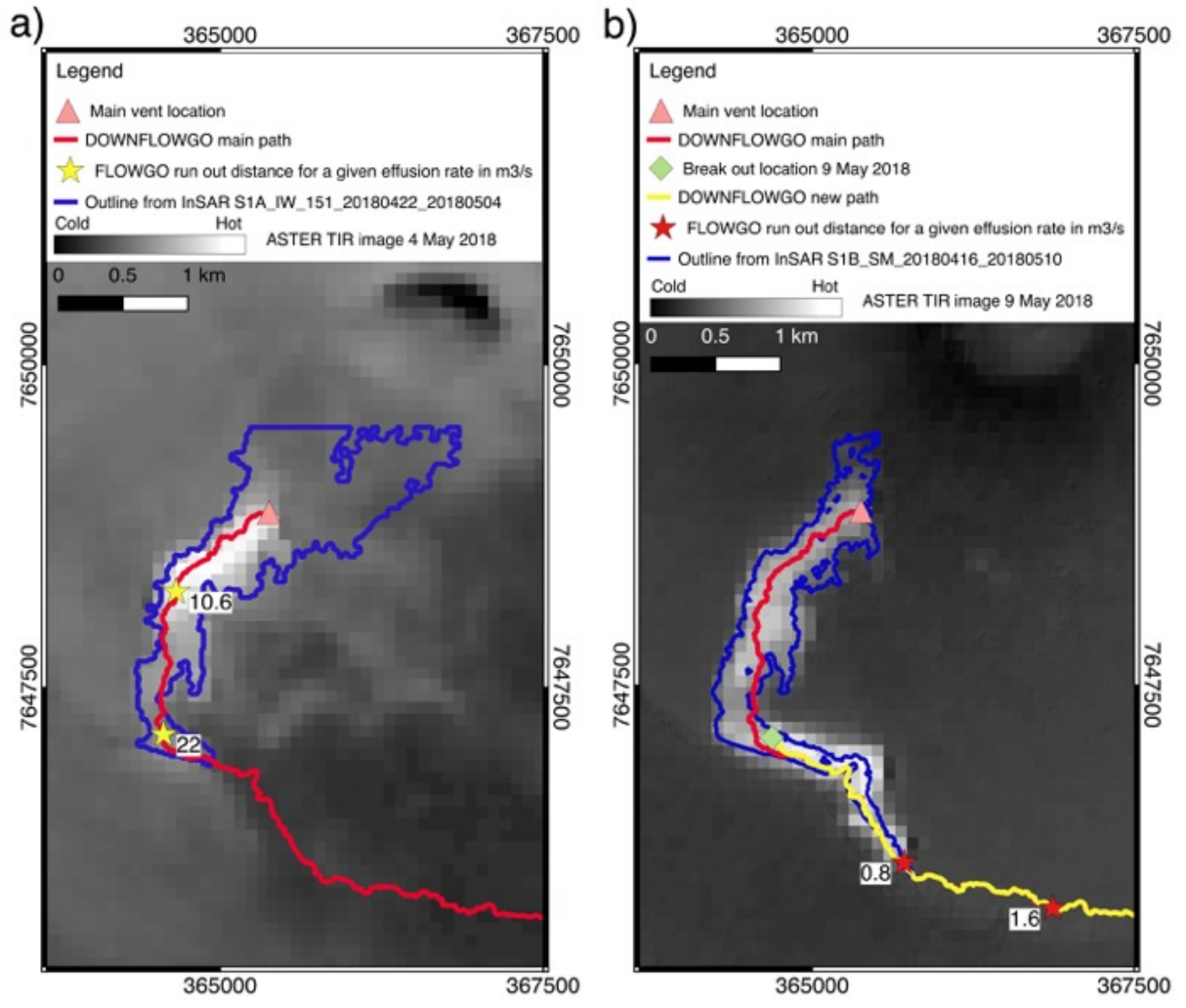
a)
365000
367500
Legend
Main vent location
DOWNFLOWGO main path
FLOWGO run out distance for a given effusion rate in m3/s
Outline from InSAR S1A_IW_151_20180422_20180504
Cold
Hot
ASTER TIR image 4 May 2018
0
0.5
1 km
7650000
7647500
10.6
22
b)
365000
367500
Legend
Main vent location
DOWNFLOWGO main path
Break out location 9 May 2018
DOWNFLOWGO new path
FLOWGO run out distance for a given effusion rate in m3/s
Outline from InSAR S1B_SM_20180416_20180510
Cold
Hot
ASTER TIR image 9 May 2018
0
0.5
1 km
7650000
7647500
0.8
1.6

Table 1. Key thermal, textural and rheological source terms used to initialize PyFLOWGO at Piton de la Fournaise as given by Chevrel et al. (2018). These are based on measurements and best-fit testing of FLOWGO on lava channels active during the December 2010 eruption of Piton de la Fournaise as described in Harris et al. (2016).

Parameter	Value	Units	Up-dated value	Source
Channel width	4	m	2 m	Updated from channel dimensions on aerial photos of 4 May
Eruption Temperature	1114	°C	1140 °C	Updated from maximum temperature data from thermal imagery of the active vent on 4 May
Phenocryst content	0.10	volume fraction	0.01 vol.%	Minimum from the 2015 lava channel
Bubble content	0.30	volume fraction	0.5 vol.%	Maximum from the 2015 lava channel
DRE Density	2970	kg/m^3		
Crust cover	100	%		
Effective Radiation Temperature	500	°C	740 °C	Mean temperature from thermal images of the south breakout channel on 4 May
Melt viscosity	Model of Villeneuve et al. (2008)	Pa s		Temperature dependent viscosity for a Piton de la Fournaise melt
Effect of crystals on mixture viscosity	Einstein Roscoe	Pa s		Valid for prolate crystal content < 0.1 (Mueller et al.2010)

Table 2. Cloud-free MODIS images processed and TADR delivered during the April-May 2018 eruption

Date & Time (UT)	Satellite	TADR (m^3/s)			Duration	Cumulative Volume ($\times 10^6$ m^3)		
(dd/mm/yyyy hh:mm)		Min.	Mid-point	Max.	(days)	Min.	Mid-point	Max.
28/04/2018 09:55	*Aqua*	11.4	16.3	21.2	0.51	0.47	0.66	0.86
28/04/2018 19:20	*Terra*	7.8	11.2	14.5	0.90	0.79	1.13	1.47
29/04/2018 21:30	*Aqua*	3.0	4.3	5.6	1.99	1.30	1.86	2.42
30/04/2018 19:05	*Terra*	3.7	5.3	6.9	2.89	1.56	2.23	2.90
02/05/2018 22:00	*Aqua*	2.5	3.6	4.6	5.01	2.13	3.05	3.96
04/05/2018 06:30	*Terra*	1.8	2.6	3.4	6.36	2.38	3.41	4.43
04/05/2018 18:40	*Terra*	2.7	3.8	4.9	6.87	2.48	3.55	4.61
04/05/2018 21:50	*Aqua*	2.8	4.0	5.2	7.00	2.51	3.59	4.67
05/05/2018 10:00	*Aqua*	1.5	2.1	2.8	7.51	2.61	3.72	4.84
05/05/2018 19:25	*Terra*	2.1	3.0	3.9	7.90	2.67	3.81	4.95
06/05/2018 06:20	*Terra*	1.3	1.8	2.4	8.36	2.73	3.91	5.08
06/05/2018 21:35	*Aqua*	1.1	1.5	2.0	8.99	2.80	4.00	5.20
07/05/2018 09:45	*Aqua*	1.4	2.0	2.7	9.50	2.85	4.08	5.30
07/05/2018 19:15	*Terra*	1.1	1.6	2.1	9.90	2.90	4.14	5.38
08/05/2018 06:10	*Terra*	0.9	1.3	1.7	10.35	2.94	4.19	5.45
08/05/2018 21:25	*Aqua*	0.6	0.9	1.1	10.99	2.98	4.25	5.53
09/05/2018 06:50	*Terra*	1.6	2.3	3.1	11.38	3.02	4.31	5.60
09/05/2018 19:00	*Terra*	2.1	3.0	3.8	11.89	3.10	4.42	5.75
10/05/2018 21:15	*Aqua*	0.9	1.2	1.6	12.98	3.23	4.62	6.01
11/05/2018 06:40	*Terra*	0.3	0.4	0.5	13.37	3.25	4.65	6.04
11/05/2018 18:50	*Terra*	1.0	1.5	1.9	13.88	3.28	4.69	6.10
12/05/2018 10:05	*Aqua*	0.4	0.6	0.8	14.51	3.32	4.75	6.17
13/05/2018 06:25	*Terra*	1.1	1.5	2.0	15.36	3.38	4.83	6.27
13/05/2018 18:35	*Terra*	1.1	1.6	2.1	15.87	3.43	4.89	6.36
13/05/2018 21:45	*Aqua*	1.0	1.5	1.9	16.00	3.44	4.91	6.39
14/05/2018 09:55	*Aqua*	1.0	1.4	1.8	16.51	3.48	4.97	6.47

14/05/2018 19:20	*Terra*	0.8	1.1	1.5	16.90	3.51	5.02	6.52
15/05/2018 06:15	*Terra*	1.4	2.0	2.6	17.35	3.55	5.08	6.60
15/05/2018 21:30	*Aqua*	0.9	1.3	1.7	17.99	3.62	5.17	6.72
16/05/2018 06:55	*Terra*	0.6	0.8	1.1	18.38	3.64	5.21	6.77
16/05/2018 19:05	*Terra*	0.9	1.3	1.6	18.89	3.68	5.25	6.83
17/05/2018 21:20	*Aqua*	0.5	0.8	1.0	19.98	3.74	5.35	6.95
19/05/2018 21:05	*Aqua*	0.4	0.5	0.7	21.97	3.82	5.46	7.10
22/05/2018 21:35	*Aqua*	0.02	0.03	0.04	24.99	3.88	5.54	7.20
24/05/2018 06:10	*Terra*	0.02	0.02	0.03	26.35	3.88	5.54	7.20

Table 3. InSAR image pairs used to produce coherence maps during the April – May eruption, and the resulting flow lengths and flow field areas. The lines entered in bold are used in the reporting form (Appendix A). Track 144 for ascending pass; 151 for descending pass.

Satellite	Mode (track)	Date (dd/mm/yyyy) Master	Date (dd/mm/yyyy) Slave	Time (UT) (hh:mm:ss)	Length (km)	Area (x 10^6 m^2)	Error (x 10^6 m^2)
S1B	**SM (151)**	**16/04/2018**	**28/04/2018**	**01:46:38**	**1.8**	**0.5**	**0.1**
S1A	**IW (144)**	**03/01/2018**	**03/05/2018**	**14:53:11**	**2.5**	**1.0**	**0.3**
S1A	IW (151)	22/04/2018	04/05/2018	01:47:32	2.6	--	--
S1B	SM (144)	27/04/2018	09/05/2018	14:52:40	3.4	1.1	0.1
S1B	**SM (151)**	**16/04/2018**	**10/05/2018**	**01:46:39**	**3.5**	**1.2**	**0.2**
S1A	IW (144)	03/01/2018	15/05/2018	14:53:12	4.0	1.2	0.2
S1A	**IW (151)**	**04/05/2018**	**16/05/2018**	**01:47:32**	**4.1**	**1.3**	**0.3**
S1B	SM (144)	27/04/2018	21/05/2018	14:52:41	4.1	--	--
S1B	SM (151)	16/04/2018	22/05/2018	01:46:39	4.1	1.3	0.1
S1A	IW (144)	03/01/2018	27/05/2018	14:53:12	4.1	1.3	0.1
S1A	IW (151)	04/05/2018	28/05/2018	01:47:33	4.1	1.3	0.1
S1B	SM (144)	27/04/2018	02/06/2018	14:52:41	--	--	--
S1B	SM (151)	16/04/2018	03/06/2018	01:46:40	--	--	--
S1A	IW (144)	03/01/2018	08/06/2018	14:53:13	4.1	--	--
S1A	IW (151)	04/05/2018	09/06/2018	01:47:34	4.1	--	--

Table 4. ASTER-URP images acquired during the eruption response. From these data, vent locations and flow field lengths were derived. Note that when the 15 m VNIR are the only data acquired because of high angle off-nadir pointing, smaller-scale features are resolved, but the dimensions of active flow features based on their thermal signature cannot be measured without the 90 m TIR data.

Date (dd/mm/yyyy)	Time (hh:mm, UT)	Mode	Vent Location (UTM)	Tube Exit Location (UTM)	Tube length (km)	Active flow length (km)	Cooling flow length (km)
02/05/2018	18:56	Night time mode (TIR only)	0365216 m E; 7648811 m S	n/a	0	0.99	1.53
04/05/2018	06:34	Daytime full mode (both VNIR and TIR)	0365261 m E; 7648841 m S	n/a	0	0.89	1.33
09/05/2018	19:03	Night time mode (TIR only)	0365261 m E; 7648841 m S	0364927 m E; 7646953 m S	0.49	1.52	1.67
11/05/2018	6:40	Daytime off-nadir pointing mode (VNIR only)	--	--	--	--	--
13/05/2018	6:28	Daytime off-nadir pointing mode (VNIR only)	--	--	--	--	--
18/05/2018	18:57	Night time mode (TIR only)	cloudy	cloudy	cloudy	cloudy	cloudy
20/05/2018	06:34	Daytime full mode (both VNIR and TIR)	cloudy	cloudy	cloudy	cloudy	cloudy
25/05/2018	19:03	Night time mode (TIR only)	0365261 m E; 7648841 m S	0364900 m E; 7647010 m S	2.07	0.63	1.08
03/06/2018	18:57	Night time mode (TIR only)	cloudy	cloudy	cloudy	cloudy	cloudy
05/06/2018	06:34	Daytime full mode (both VNIR and TIR)	Post-eruption	Post-eruption	Post-eruption	Post-eruption	Post-eruption
19/06/2018	18:57	Night time mode (TIR only)	Post-eruption	Post-eruption	Post-eruption	Post-eruption	Post-eruption

LAVA FLOW FIELD REPORTING FORM (file name save format: yyyymmdd-Volcano name-ANR-LAVA-REPORT-##)	
Target	<VOLCANO NAME>
Eruption Start Date and Time (local)	<yyyy-mm-dd-T-hh-mm> (local time)
Report Initialization Date and Time (UTC)	<yyyy-mm-dd-T-hh-mm> (GMT)
Reporting form initialized by	<SURNAME> <name>

Field 1: TIME-AVERAGED DISCHARGE RATE	
Sensor	<Sensor name>
Processing System	<Hot spot detection system>
Last update	<yyyy-mm-dd-T-hh-mm>
Up-dated by	<SURNAME> <name>

Image Date	Image Time	TADR-min	TADR-max
<yyyy-mm-dd>	<hh-mm>	<m^3/s>	<m^3/s>
<yyyy-mm-dd>	<hh-mm>	<m^3/s>	<m^3/s>
<yyyy-mm-dd>	<hh-mm>	<m^3/s>	<m^3/s>
<yyyy-mm-dd>	<hh-mm>	<m^3/s>	<m^3/s>
<yyyy-mm-dd>	<hh-mm>	<m^3/s>	<m^3/s>
<yyyy-mm-dd>	<hh-mm>	<m^3/s>	<m^3/s>
<yyyy-mm-dd>	<hh-mm>	<m^3/s>	<m^3/s>
<yyyy-mm-dd>	<hh-mm>	<m^3/s>	<m^3/s>
<yyyy-mm-dd>	<hh-mm>	<m^3/s>	<m^3/s>
<yyyy-mm-dd>	<hh-mm>	<m^3/s>	<m^3/s>

Comments:

<free text>

Time Series:

Start date	Current date	No. data points	Duration
<yyyy-mm-dd>	<yyyy-mm-dd>	<##>	<days>

<place time-series graph here>
Y1-axis = "TADR (m^3/s); Y2-axis = "Volume ($\times 10^6$ m^3)"; x-axis "Date (mm-dd)"

Field 2: FLOW SIMULATION			
Last update		<yyyy-mm-dd-T-hh-mm>	
Up-dated by		<SURNAME> <name>	
Flow path model		<model name>	
DEM date	DEM resolution	Noise	No. iterations
<yyyy-mm-dd>	<m>	<±m>	<##>
Vent location	Source: airborne GPS	Source: field GPS	Source: ASTER
<UTM>	<Y/N>	<Y/N>	<Y/N>
<GOOGLE?>	<yyyy-mm-dd>	<hh-mm> (local time)	
Flow length model		<model name>	
Initialization file		<file name>	
Run Date	TADR used	Channel dimension	Run out
<yyyy-mm-dd>	<m^3/s>	<m>	<m>
<yyyy-mm-dd>	<m^3/s>	<m>	<m>
<yyyy-mm-dd>	<m^3/s>	<m>	<m>
<yyyy-mm-dd>	<m^3/s>	<m>	<m>
<yyyy-mm-dd>	<m^3/s>	<m>	<m>
<yyyy-mm-dd>	<m^3/s>	<m>	<m>
<yyyy-mm-dd>	<m^3/s>	<m>	<m>
Flow projection map:			
Vent position	Current run date	TADR used	Eruption temperature
<UTM>	<yyyy-mm-dd>	<m^3/s>	<°C>
<place PYFLOWGO output here> PYFLOWGO parameter output screen		<place map output here> DOWNFLOW paths with FLOWGO distances on shaded relief	
Comments: <free text>			

Field 3: ASTER			
Last update		<yyyy-mm-dd-T-hh-mm>	
Up-dated by		<SURNAME> <name>	
Image date	Image time (UT)	TADR	SO_2 flux
<yyyy-mm-dd>	<hh-mm>	<m^3/s>	<kg/s>
<yyyy-mm-dd>	<hh-mm>	<m^3/s>	<kg/s>
<yyyy-mm-dd>	<hh-mm>	<m^3/s>	<kg/s>
<yyyy-mm-dd>	<hh-mm>	<m^3/s>	<kg/s>
Image date	Image time (UT)	Anomaly Length	Anomaly Area
<yyyy-mm-dd>	<hh-mm>	<m>	<m^2>
<yyyy-mm-dd>	<hh-mm>	<m>	<m^2>
<yyyy-mm-dd>	<hh-mm>	<m>	<m^2>
<yyyy-mm-dd>	<hh-mm>	<m>	<m^2>
ASTER hot spot map:			
Image date	Image time (UT)	VNIR bands used	TIR bands used
<yyyy-mm-dd>	<hh-mm>	<b#; b#; b#>	<b#; b#; b#>
<ASTER VNIR image> contrast enhanced, density sliced ASTER image on Google Earth		<ASTER TIR image> contrast enhanced, density sliced ASTER image on Google Earth	
Comments: <free text>			

Field 4: INSAR				
Last update			<yyyy-mm-dd-T-hh-mm>	
Up-dated by			<SURNAME> <name>	
Processing System			<InSAR processing system>	
	Satellite	Mode	Date	time
Master	<sat>	<mode>	<yyyy-mm-dd>	<hh-mm>
Slave	<sat>	<mode>	<yyyy-mm-dd>	<hh-mm>
Dimensions:	Length =	<m>	Area =	<m^2>
Master	<sat>	<mode>	<yyyy-mm-dd>	<hh-mm>
Slave	<sat>	<mode>	<yyyy-mm-dd>	<hh-mm>
Dimensions:	Length =	<m>	Area =	<m^2>
Master	<sat>	<mode>	<yyyy-mm-dd>	<hh-mm>
Slave	<sat>	<mode>	<yyyy-mm-dd>	<hh-mm>
Dimensions:	Length =	<m>	Area =	<m^2>
Master	<sat>	<mode>	<yyyy-mm-dd>	<hh-mm>
Slave	<sat>	<mode>	<yyyy-mm-dd>	<hh-mm>
Dimensions:	Length =	<m>	Area =	<m^2>
InSAR coherence and flow area maps:				
	Satellite	Mode	Date	time
Master	<sat>	<mode>	<yyyy-mm-dd>	<hh-mm>
Slave	<sat>	<mode>	<yyyy-mm-dd>	<hh-mm>

< coherence image >	<lava flow outline and length path>

Comments:

<free text>

Appendix B

InSAR data processing

The InSAR method consists of computing an interferogram by subtracting the phase between two SAR images acquired of the same area at different epochs. The phase recorded on a SAR image depends both on the radar wave round trip travel time between the instrument and the ground, and on the interaction between the radar wave and reflectors on the ground surface. Provided that this last component remains stable between two successive acquisitions, the differential phase displayed on the interferogram will only reflect changes in the radar wave travel time between the two acquisitions and can be exploited to measure possible ground surface displacement occurring between the two acquisitions. This is the classical application of InSAR that has seen a succesful development in the field of volcanological application since the pioneering work of Massonnet et al. (1995) (e.g., Biggs and Pritchard 2017; Pinel, Poland, and Hooper 2014; Massonnet, Briole, and Arnaud 1995; Ferretti, Prati, and Rocca 2001; Hooper et al. 2004).

If the geometry or dielectrical properties of the reflectors on the ground change significantly between the two radar acquisitions, the differential phase will appear very noisy ("decorrelated" or "incoherent") on the interferogram, making it unexploitable for displacement measurement. This generally occurs when the ground is covered by dense vegetation, the geometric properties of individual plants changing very quickly due to continuous growth or to the motion of leavees in the wind. It could also occur when heavy rain, snow fall, strong erosional events, air fall (in volcanic context) occurs between the two radar acquisitions. Interferometric coherence provides an estimation of the temporal stability of the ground contribution to phase measurement. It is generaly derived as an inverse function of the phase variance calculated between neighboring pixels (e.g., in a 3 × 3 pixels box) in the interferogram and is usualy represented as an image where very coherent pixels have values close to one and poorly coherent pixels have values close to zero.

If a lava flow is emplaced between two successive SAR acquisitions, the interferometric coherence will be very low in the area covered by the lava flow due to the change in the geometry of the ground reflectors there. If, in contrast, the surrounding area remains coherent on the interferogram (i.e., if the lava flow is emplaced on bare rock or soil), the lava flow will appear on the interferometric coherence image as a black area surrounded by lighter-toned pixels. This is typicaly the case at Piton de la Fournaise when a lava flow is emplaced in the (largely) vegetation-free Enclos Fouqué caldera (the upper part of the volcano) where the interferometric coherence is very high (>70 %). Here, by detecting the boundary between dark and light-toned areas one can obtain a map of the lava flow contour (e.g., Rowland et al. 2003; Dietterich et al. 2012; Bato et al. 2016).

In this study, we exploited interferometric coherence images to produce an early map of the April-May 2018 lava flow. To provide relevant data for input in the response protocol in as timely fashion as possible, we used only ESA Sentinel-1 data. Sentinel-1A/B data are acquired for La Réunion island every six days both during ascending and descending passes, alternatively in Interferometric Wide Swath mode (IW, range spacing = 2.33 m, azimuth spacing = 14.06 m) and in Stripmap mode (SM, range spacing = 2.66 m, azimuth spacing = 4.15 m). The data are made freely available by the European Space Agency (ESA) via the Sentinel-1 Data Hub between 4 and 24 hours after acquisition.

As it is not possible to produce an interferogram by combining IW with SM data, so the shortest time period between two usable interferograms is 12 days. We compute the interferograms and the coherence images using the Doris 5.0.3 InSAR processor (Kampes and Usai 1999; Kampes and Hanssen 2003). To georeference the interferometric products, we used a 5 m resolution Digital Elevation Model (DEM) produced by the French Geographic Institute from two airborne LiDAR sur-

veys carried out over La Réunion in 2008 and 2009. After georeferencing, the coherence maps derived from IW data have a 15 m pixel size, and those derived from SM data have a 5 m pixel size.

To discriminate, in the coherence images, areas covered by lava flow from other poorly coherent areas (e.g., due to air fall or to changes in the soil moisture between the two radar acquisitions) we developed a three step procedure. The first step consists of applying a median filter on the coherence image. Then, in a second step, we perform a clustering-based image thresholding approach: the Otsu algorithm (Otsu 1979). The resulting binary image is used to trace the lava flow boundary (including boundaries of kipukas) using the bwboundaries Matlab© function. Finally, the lava flow surface area is estimated with associated uncertainty taking into account the pixel surface and the probability that each pixel belongs to the lava flow knowing its coherence.

As the April – May 2018 eruption lasted more than one month, we were able to compute several coherence images combining, for a given acquisition geometry and mode (ascending or descending pass, IW or SM mode), a unique master image with several slave images. The master images were acquired before the beginning of the eruption and the slave images during the eruption, or just after its end. This allowed us to estimate the evolution of the lava flow surface area at different epochs (see Appendix D). Moreover, several interferograms, spanning the total duration of the eruption, were produced by combining a master image acquired before the beginning of the eruption and the slaves images acquired in the weeks following the end of the eruption. The coherence images associated with these interferograms have been stacked to produce an accurate map of the final lava flow extension and its total surface area (see Appendix D).

Generaly, the lava flow field becomes coherent a few weeks to a few months after the end of the eruption (Bato et al. 2016; Chaussard 2016; Wittmann, Sigmundsson, and Lavallée 2017). The thickness of the lava flow field can be estimated from the topographical residuals in the interferograms. These residuals reflect the deviation between a reference DEM used in the interferometric processing and the actual topography (Massonnet and Feigl 1998). Since the amplitude of topographic residuals is proportional to the perpendicular baseline of the interferometric couple (Massonnet and Feigl 1998), one can obtain a relatively accurate determination of the changes in the volcano topography due to lava flow emplacement by a statistical exploitation of several interferograms covering a large range of perpendicular baseline (Bato et al. 2016). The lava thickness obtained in this way can be used not only to evaluate the volume of the lava flow field, and then, by making some assumptions on the lava porosity, the volume of lava emitted, but also to update the DEM after each eruption. Such an update is mandatory to achieve model-based flow-length projections. Unfortunately, in the case of the April 2018 eruption, we could not use the Sentinel-1 interferograms to determine the lava flow thickness since the perpendicular baseline (B_{perp}) of the S1 interferometric couples was always very low ($\overline{B_{perp}} = 48\ \text{m} \pm 35\ \text{m}$). A particular effort has been made by ESA in the Sentinel-1 system design to achieve an orbital tube of 50 m radius (rms). This guaranties high performances for ground surface displacement measurement purposes by reducing the sensibility of the interferograms to possible topographic artifacts. However, in our case, this "improvement" is a disadvantage since we are looking for topographic residuals (Ebmeier et al. 2012; Albino et al. 2015; Kubanek, Westerhaus, et al. 2015; Kubanek, Richardson, et al. 2015; Bato et al. 2016; Kubanek, Westerhaus, and Heck 2017). The characteristics of CosmoSky-Med and TerraSAR-X/TanDEM-X constellations make them better suited for this type of application. The use of future CSK and TSX/TDX acquisitions for Piton de la Fournaise will allow us to calculate the April-May 2018 lava flow thickness.

References

Albino, F, B Smets, N Oreye, and F Kervyn. 2015. "High-Resolution TanDEM-X DEM : An Accurate Method to Estimate Lava Flow Volumes at Nyamulagira." *Journal of Geophysical Research : Solid Earth*, 4189–4207. doi:10.1002/2015JB011988.Received.

Bato, M. G., J. L. Froger, A. J. L. Harris, and N. Villeneuve. 2016. "Monitoring an Effusive Eruption at Piton de La Fournaise Using

Radar and Thermal Infrared Remote Sensing Data: Insights into the October 2010 Eruption and Its Lava Flows." *Geological Society, London, Special Publications*. doi:10.1144/SP426.30.

Biggs, Juliet, and Matthew E. Pritchard. 2017. "Global Volcano Monitoring: What Does It Mean When Volcanoes Deform?" *Elements* 13 (1): 17–22. doi:10.2113/gselements.13.1.17.

Chaussard, Estelle. 2016. "Subsidence in the Paricutin Lava Field: Causes and Implications for Interpretation of Deformation Fields at Volcanoes." *Journal of Volcanology and Geothermal Research* 320: 1–11. doi:10.1016/j.jvolgeores.2016.04.009.

Dietterich, Hannah R., Michael P. Poland, David A. Schmidt, Katharine V. Cashman, David R. Sherrod, and Arkin Tapia Espinosa. 2012. "Tracking Lava Flow Emplacement on the East Rift Zone of Klauea, Hawaii, with Synthetic Aperture Radar Coherence." *Geochemistry, Geophysics, Geosystems* 13 (5): 1–17. doi:10.1029/2011GC004016.

Ebmeier, S. K., J. Biggs, T. A. Mather, J. R. Elliott, G. Wadge, and F. Amelung. 2012. "Measuring Large Topographic Change with InSAR: Lava Thicknesses, Extrusion Rate and Subsidence Rate at Santiaguito Volcano, Guatemala." *Earth and Planetary Science Letters* 335–336. Elsevier: 216–25. doi:10.1016/j.epsl.2012.04.027.

Ferretti, Alessandro, Claudio Prati, and Fabrio Rocca. 2001. "Permanent Scatters in SAR Interferometry." *IEEE Transactions on Geoscience and Remote Sensing* 39 (1): 8–20. doi:10.1109/36.898661.

Hooper, Andrew, Howard Zebker, Paul Segall, and Bert Kampes. 2004. "A New Method for Measuring Deformation on Volcanoes and Other Natural Terrains Using InSAR Persistent Scatterers." *Geophysical Research Letters* 31 (23): 1–5. doi:10.1029/2004GL021737.

Kampes, Bert, and Ramon Hanssen. 2003. "Radar Interferometry with Public Domain Tools." In *Proceedings of FRINGE 2003*.

Kampes, Bert, and Stefania Usai. 1999. "Doris: The Delft Object-Oriented Radar Interferometric Software." In *Proceedings ITC 2nd ORS Symposium*.

Kubanek, Julia, Jacob A. Richardson, Sylvain J. Charbonnier, and Laura J. Connor. 2015. "Lava Flow Mapping and Volume Calculations for the 2012–2013 Tolbachik, Kamchatka, Fissure Eruption Using Bistatic TanDEM-X InSAR." *Bulletin of Volcanology* 77 (12): 1–13. doi:10.1007/s00445-015-0989-9.

Kubanek, Julia, Malte Westerhaus, and Bernhard Heck. 2017. "TanDEM-X Time Series Analysis Reveals Lava Flow Volume and Effusion Rates of the 2012–2013 Tolbachik, Kamchatka Fissure Eruption." *Journal of Geophysical Research: Solid Earth* 122 (10): 7754–74. doi:10.1002/2017JB014309.

Kubanek, Julia, Malte Westerhaus, Andreas Schenk, Nurnaning Aisyah, Kirbani Sri Brotopuspito, and Bernhard Heck. 2015. "Volumetric Change Quantification of the 2010 Merapi Eruption Using TanDEM-X InSAR." *Remote Sensing of Environment* 164. Elsevier Inc.: 16–25. doi:10.1016/j.rse.2015.02.027.

Massonnet, Didier, Pierre Briole, and Alain Arnaud. 1995. "Deflation of Mount Etna Monitored by Spaceborne Radar Interferometry." *Nature* 375: 375–567.

Massonnet, Didier, and Kurt L Feigl. 1998. "Radar Interferometry and Its Application to Changes in the Earth's Surface." *Reviews of Geophysics* 36 (4): 441–500. doi:10.1029/97RG03139.

Otsu, Nobuyuki. 1979. "A Threshold Selection Method from Gray-Level Histograms." *IEEE Transaction on Systems, Man and Cybernetics* SMC-9 (1): 62–66.

Pinel, V., M. P. Poland, and A. Hooper. 2014. "Volcanology: Lessons Learned from Synthetic Aperture Radar Imagery." *Journal of Volcanology and Geothermal Research* 289. Elsevier B.V.: 81–113. doi:10.1016/j.jvolgeores.2014.10.010.

Rowland, Scott K., Andrew J.L. Harris, Martin J. Wooster, Falk Amelung, Harold Garbeil, Lionel Wilson, and Peter J. Mouginis-Mark. 2003. "Volumetric Characteristics of Lava Flows from Interferometric Radar and Multispectral Satellite Data: The 1995 Fernandina and 1998 Cerro Azul Eruptions in the Western Galápagos." *Bulletin of Volcanology* 65 (5): 311–30. doi:10.1007/s00445-002-0262-x.

Wittmann, Werner, Freysteinn Sigmundsson, and Yan Lavallée. 2017. "Post-Emplacement Cooling and Contraction of Lava Flows : InSAR Observations and a Thermal Model for Lava Fields at Hekla Volcano , Iceland." *Journal of Geophysical Research B: Solid Earth*, 1–20. doi:10.1002/2016JB013444.Abstract.

Appendix C

Example of ASTER URP email

Given here is an example of the ASTER URP trigger for April–May 2018 eruption of Piton de la Fournaise as triggered by the University of Hawaii's hot spot detection system, MODVOLC (Wright et al. 2002):

From:	Thermal Hotspot Work <thermal@hotspot3.higp.soest.hawaii.edu>
Sent:	Saturday, April 28, 2018 3:25 PM
To:	daac_alerts2@higp.hawaii.edu
Subject:	HIGP Urgent Request

Mike|Ramsey|Hawaii Institute of Geophysics and Planetology

|Volcano|1|21.24|1|55.71|Fournaise,_Piton_de_la|Fournaise,_Piton_de_la|

http://modis.higp.hawaii.edu/cgi-bin/mergeimage?maptype=relief&jyear=2018&jday=116&jperiod=4.0&lonmin=55.658&lonmax=55.758&latmin=-21.294&latmax=-21.194&xsize=600&ysize=600

|Indian_Ocean_(western)|Middle_East_and_Indian_Ocean|Day|fullmode|Yes|Normal|Yes|Normal|Normal|Normal|Normal|Normal|Normal|Normal|Normal|Normal|UTM

|Cubic Convolution|Immediately on receipt of data|||Volcano monitoring|HIGP Urgent Request

|mramsey@pitt.edu

The automatic response to this notification from the URP system was as follows :

From:	aesics@usgs.gov <aesics@usgs.gov>
Sent:	Saturday, April 28, 2018 3:31 PM
Subject:	AESICS - New Request: Fournaise,_Piton_de_la

A new request has been received by AESICS and is pending approval. The full request details and/or update the request, click here.

Overview

DAAC ID: 26392
STAR ID: None
Event Name: Fournaise,_Piton_de_la
Application: Volcano
Justification: Volcano monitoring

Location

Event Country: Indian_Ocean_(western)
Event Location: Middle_East_and_Indian_Ocean
Coordinates: (-21.24, 55.71)
Reference URL: Link

Acquisition and Processing

Sensor Mode: full mode
Local Time: Night
Off-NADIR Ok: yes
Off-NADIR Amount: Normal
Processing Urgency: Expedited

Gain Settings

VNIR1: normal
VNIR2: normal
VNIR3: normal
SWIR4: normal
SWIR5: normal
SWIR6: normal
SWIR7: normal
SWIR8: normal
SWIR9: normal

LAVA FLOW FIELD REPORTING FORM (file name save format: yyyymmdd-Volcano name-ANR-LAVA-REPORT-##)			
Target		Piton de la Fournaise	
Eruption Start Date and Time (local)		2018-04-27-T-23:50 (local time)	
Report Date and Time (UTC)		2018-07-11-T-12:00 (GMT)	
Up-dated by		HARRIS Andrew	
Field 1: TIME-AVERAGED DISCHARGE RATE			
Sensor		MODIS	
Processing System		MIROVA	
Last update		2018-05-24T06:10:00	
Up-dated by		COPPOLA Diego	
Image Date	Image Time	TADR-min	TADR-max
15-05-2018	06:15:00	1.32	2.71
15-05-2018	21:30:00	0.88	1.81
15-05-2018	21:30:00	0.88	1.81
16-05-2018	06:55:00	0.53	1.09
16-05-2018	19:05:00	0.82	1.69
16-05-2018	19:05:00	0.82	1.69
17-05-2018	21:20:00	0.51	1.05
19-05-2018	21:05:00	0.35	0.73
22-05-2018	21:35:00	0.02	0.04
24-05-2018	06:10:00	0.02	0.03

Comments:

The MODIS image acquired today at 06:10 UTC, indicates very low levels of thermal activity over the lava field (~5 MW) corresponding to a very low TADR (0.015 to 0.03 m^3/s). However, this low thermal flux could be also related to the cooling of the lava field emplaced in the previous days; meaning there is the possibility that there is no flow so the TADR is “false”; it being derived from a cooling anomaly.

Time Series:			
Start date	Current date	No. data points	Duration
2018-04-27T21:45	2018-05-24T06:10	35	27

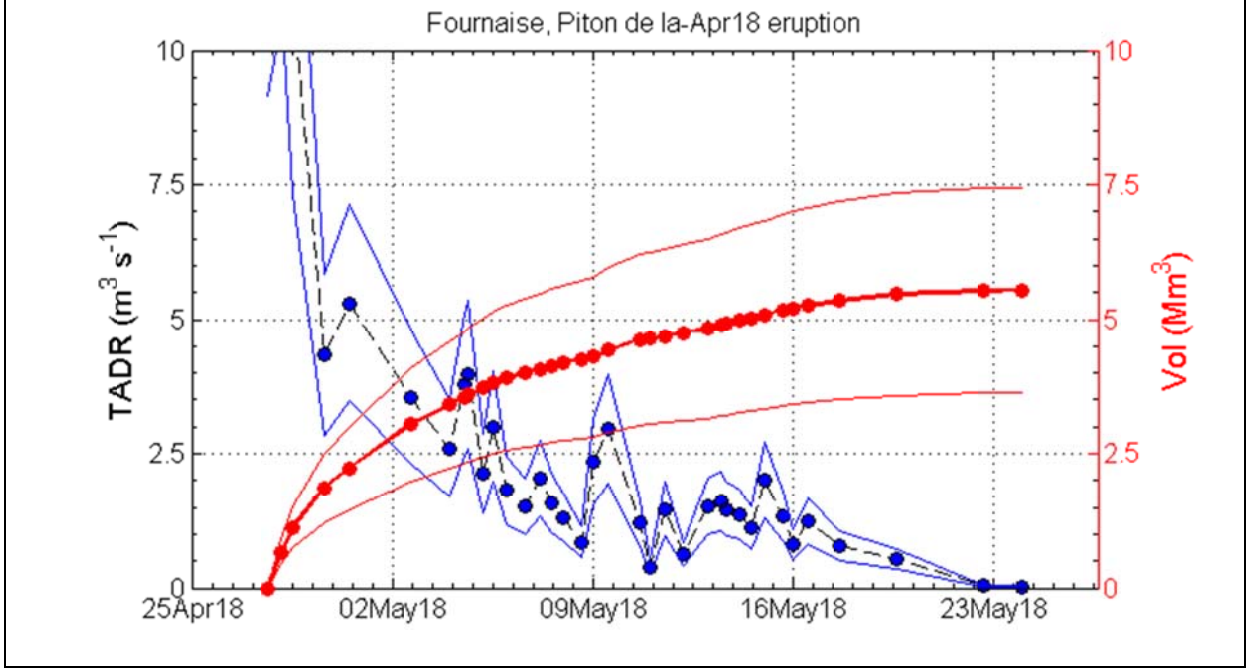

Field 2: FLOW SIMULA TION			
Last update		<2018-06-21-T-15-00>	
Up-dated by		CHEVREL Oryaëlle	
Flow path model		DOWNFLOW	
DEM file	DEM resolution	Noise	No. iterations
5m_updated.asc	5 m	±0.001 – 1m	1000
Vent location	Source: airborne GPS	Source: field GPS	Source: ASTER
365377; 7648853	N	Surveillance camera	N
40 K (Google Earth)	2018-04-28	04:33 (local time)	OVPF
Flow length model		PyFLOWGO	
Initialization file		Same as 2010 eruption	
Run Date	TADR used	Channel dimension	Run out
2018-06-22	20m^3/s	3 × 1.5	1100 m
Flow projection map:			
Vent position	Current run date	TADR used	Eruption temperature
365377; 7648853<UTM>	2018-06-22	20 m^3/s	1114°C

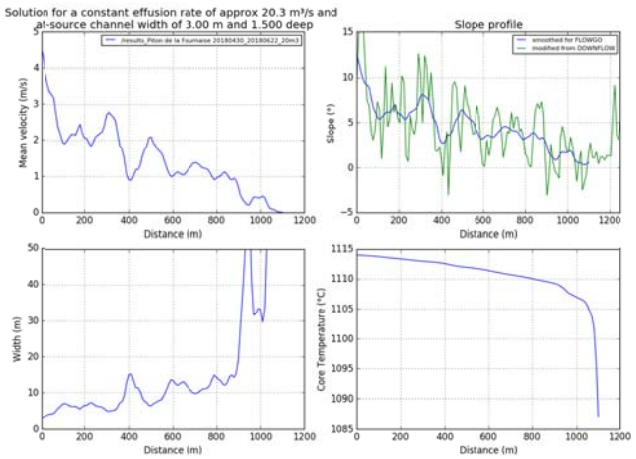

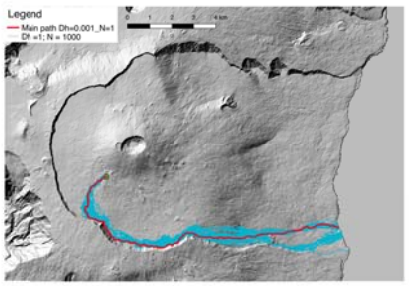

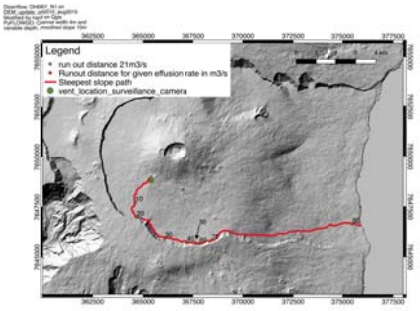

Comments:

Initial vent position is based on the middle of the main fissure as apparent in the web-cam data and projected onto GOOGLE EARTH. This will need checking and updating : **TREAT WITH CAUTION**

The DOWNFLOW path has been modified by hand to remove the lava ponding effect (green in graph) and then the slope was smoothed every 10 m (blue in graph).

Field 3: ASTER			
Last update		<2018-05-24T06:10:00>	
Up-dated by		RAMSEY Michael	
Image date	Image time (UT)	TADR (m^3/s)	SO_2 flux (kg/s)
04-05-2018	06:34:00	*not calculated*	*not calculated*
Image date	Image time (UT)	Anomaly Length (m)	Anomaly Area (m^2)
02-05-2018	06:15:00	1367	281,411
04-05-2018	06:34:00	2446	553,918
09-05-2018	19:03:00	4107	1,098,212
25-05-2018	19:03:00	4301	973,751
ASTER hot spot map:			
Image date	Image time (UT)	VNIR bands used	TIR bands used
04-05-2018	06:34:00	<b3; b2; b1>	b13 / b13; b11; b10

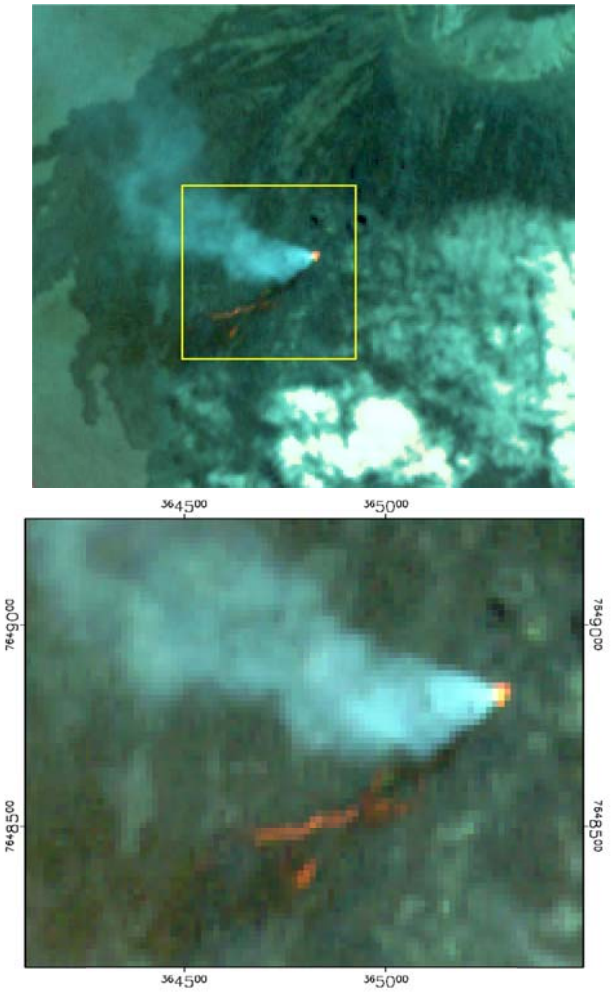

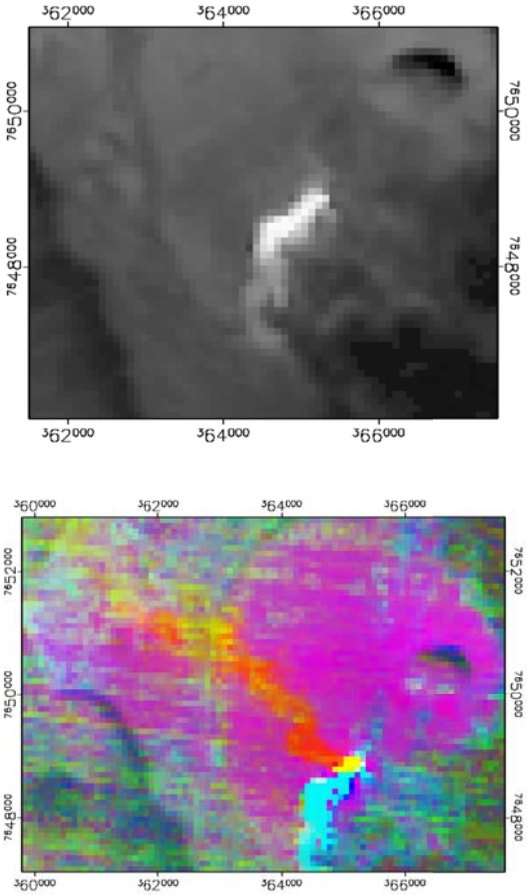

Comments:

4 May 2018 ASTER VNIR (left) and TIR (right) data shown. First ASTER full mode (VNIR + TIR) acquisition following URP trigger. Vent location verified in the VNIR data along with the presence of open channels. TIR anomaly length + area includes all pixels above background, not just the saturated pixels corresponding to open channel location. TIR decorrelation stretch color composite confirms SO_2 in plume (yellow/orange). Note: TADR and SO_2 flux values were not calculated.

Field 4: INSAR				
Last update			2018-07-06-T-15-00	
Up-dated by			Alexis HRYSIEWICZ	
Processing System			Doris 5.0 and Matlab	
	Satellite	Mode (track)	Date	time
Master	S1B	SM (151)	2018-04-16	01:46:38.148088
Slave	S1B	SM (151)	2018-04-28	01:46:38.734417
Dimensions:	Length =	1.8 km	Area =	$0.5 \times 10^6 m^2 \pm 0.1 \times 10^6$
Master	S1A	IW (144)	2018-01-03	14:53:10.372910
Slave	S1A	IW (144)	2018-05-03	14:53:11.013571
Dimensions:	Length =	2.5 km	Area =	$1 \times 10^6 m^2 \pm 0.3 \times 10^6$
Master	S1B	SM (151)	2018-04-16	01:46:38.148088
Slave	S1B	SM (151)	2018-05-10	01:46:39.238256
Dimensions:	Length >	3.5 km	Area =	$1.2 \times 10^6 m^2 \pm 0.2 \times 10^6$
Master	S1A	IW (151)	2018-05-04	01:47:32.171178
Slave	S1A	IW (151)	2018-05-16	01:47:32.875454
Dimensions:	Length =	4.1 km	Area =	$1.3 \times 10^6 m^2 \pm 0.3 \times 10^6$
InSAR coherence and flow area maps:				
	Satellite	Mode	Date	time
Master	S1B	SM (144)	2018-04-27	14:52:39.557416
Slave	S1B	SM (144)	2018-06-26	14:52:43.052570

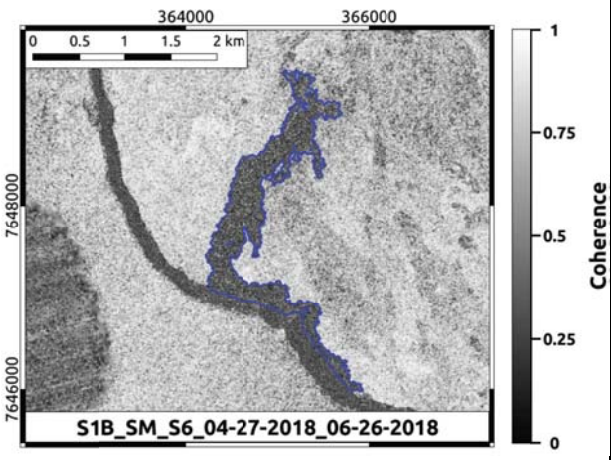

Fig 1: Coherence image between April 27, 2018 and June 26, 2018. The final lava flow contour extracted from InSAR is given with the blue line.

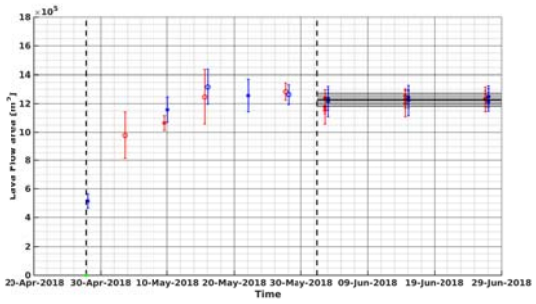

Fig 2: Evolution of the lava flow area from InSAR. The stars correspond to the Sentinel 1 SM data, the circles are for the Sentinel 1 IW data. The blue color is used to denote the Descending acquisitions, and the red is for Ascending images. The black line is the final computed area obtained from several coherence images covering the entire eruption duration. The error bars are set as two times the standard deviation. The gray zone marks the uncertainty on the final area.

Comments: